The Dissertation Committee for Carl Oliver Knutson
certifies that this is the approved version of the following dissertation:

Magnetic Domain Wall Dynamics in Nanoscale Thin Film Structures

Committee:

Maxim Tsoi, Supervisor

Paul Barbara

James Erskine

John Markert

Jack Swift

Magnetic Domain Wall Dynamics in Nanoscale Thin Film Structures

by

Carl Oliver Knutson, B.S.

DISSERTATION

Presented to the Faculty of the Graduate School of

The University of Texas at Austin

in Partial Fulfillment

of the Requirements

for the Degree of

DOCTOR OF PHILOSOPHY

THE UNIVERSITY OF TEXAS AT AUSTIN

May 2008

Dedicated to my wife Laura.

Acknowledgments

I would like to thank my advisor, Maxim Tsoi, for his guidance and support. A special thanks goes to Geoff Beach for all of his insight and assistance. Thanks to Corneliu Nistor for showing me the ropes on the MOKE system. Thanks to Mike Tiner for providing tech support every time the FIB would break down. Additional thanks go to the members of my dissertation committee: James L. Erskine, John Markert, Paul Barbara, and Jack Swift.

Thanks to all my friends for providing distraction when I needed it and even when I didn't need it. Thanks to my parents for encouraging my interest in science from the beginning. Thank you to Laura for all her love, companionship, and encouragement through the years.

Carl Oliver Knutson

The University of Texas at Austin

May 2008

Magnetic Domain Wall Dynamics in Nanoscale Thin Film Structures

Publication No. _____

Carl Oliver Knutson, Ph.D.
The University of Texas at Austin, 2008

Supervisor: Maxim Tsoi

The dynamics of individual magnetic domain walls in permalloy nanowires fabricated through focused ion beam patterning is presented in this dissertation. The motion of an individual domain wall is detected directly via magneto-optical Kerr polarimetry. In the basic measurement, the velocity of the domain wall is measured over a range of external driving magnetic fields. The velocity measurement is found to have two distinct linear regions separated by a region with a negative differential. This measurement is then expanded upon by varying the width of the nanowire and applying a DC current though the nanowire.

The means by which the domain wall enters the nanowire from a continuous film is investigated. A pinning potential traps the domain wall at the interface between the nanowire and continuous film at low magnetic fields. Fields below the critical "injection" field allow the domain wall to overcome

the pinning potential through a thermal activation mechanism. The critical injection field is found to depend on the width of the nanowire.

A moving domain wall has been found to create a voltage across the nanowire through which it traverses. The voltage produced is proportional to the velocity of the domain wall and is on the order of hundreds of nV.

Table of Contents

Acknowledgments **v**

Abstract **vi**

List of Figures **x**

Chapter 1. Introduction **1**
1.0.1 Outline 1

Chapter 2. Background Theory **3**
2.1 Ferromagnetism Basics 3
2.2 Magnetic Domain Walls 6
2.3 Magnetic Domain Wall Dynamics 10
2.4 The Magneto-optical Kerr Effect 11

Chapter 3. Experimental Setup **14**
3.1 Device Fabrication via Focused Ion Beam Patterning 14
3.2 Magnetization Measurements with a MOKE Polarimeter . . . 20
3.2.1 Polarimeter Optics and Signal Acquisition 23
3.2.2 Polarimeter Magnet System 24

Chapter 4. Domain Wall Dynamics **27**
4.1 Measurement Methods 28
4.2 Field Driven Domain Wall Dynamics 33
4.2.1 Model for Domain Wall Motion 33
4.2.2 Domain Wall Mobility Measurement 41
4.3 Domain Wall Dynamics in Nanowires of Varying Width 45
4.4 Current Driven Domain Wall Dynamics 47
4.4.1 Current Induced Torques on Domain Walls 48
4.4.2 Current Driven Mobility Measurements 49

Chapter 5. Domain Wall Injection **56**
5.1 Injection via Thermal Activation 56
5.2 Injection and Nanowire Width 64

Chapter 6. Domain Wall Induced Voltage **70**
6.1 Measurement Methods 71
6.2 Results and Discussion 73

Chapter 7. Conclusions **85**
7.0.1 Recommendations for Future Work 87

Bibliography **89**

Vita **97**

List of Figures

2.1 A single domain structure (a) will have large stray fields. The stray fields are minimized by the formation of closure domains (b). 7

2.2 The two types of domain walls (a), Bloch and Néel. The red dotted lines represent the edges of the domain walls. Néel walls are generally present in thin films. In a strip of magnetic thin film (b) Néel domain walls, represented by the blue line, will generally form either a head-to-head or a tail-to-tail domain wall. 8

2.3 The spin angle distribution in a domain wall in a material with uniaxial anisotropy. The dotted line represents the effective domain wall width. 9

2.4 The three MOKE geometries describe the relative orientation between the magnetization of the material and the polarized light source. The three geometries are polar, transverse, and longitudinal. The rotation of the polarization of the light source, in this case a polarized laser indicated by the red line in a plane perpendicular to the material, depends on the magnetization of the material. 13

3.1 A schematic of material removed from the continuous permalloy film resulting in a nanowire of width w. The larger rectangular areas are removed using the normal raster mode. The areas along the nanowire edges are removed via the cleaning cross section mode with the final line of material removed forming the edge of the nanowire. 16

3.2 An example of a nanowire with one end cut created by removing material from a permalloy film using a focused ion beam. This configuration is used to study a single domain wall. 17

3.3 A nanowire with both ends connected created by removing material from a permalloy film using a focused ion beam. This configuration can be used to study domain wall dynamics under the influence of current by electrically isolating one end of the nanowire from the other. 18

3.4 A contact pad made with FIB in a permalloy film. The dimensions of this contact pad are of sufficient size to allow a wire bond contact to be applied for current measurements. 19

3.5 Nanomanipulator probes inside the FIB chamber allow for *in situ* electrical measurements. Here the probes are configured for a four probe resistance measurement. 21

3.6 A schematic of the components for the MOKE polarimeter. . . 22

4.1 The magnetic susceptibility and SEM images of a nanowire. The susceptibility signal is the result of a lock-in amplifier measuring the MOKE signal at the frequency of a saturating square wave magnetic field. The darkest coloration in the susceptibility image represents a lack of MOKE signal. 30

4.2 Kerr signal transients measured along a nanowire. As the laser spot moves along the nanowire the time of reversal increases. The position and reversal time data is then used to calculate the domain wall velocity. 32

4.3 The configuration of the magnetization in a Néel domain wall at zero applied field and with a non-zero applied field. The red lines represent the edges of the domain wall. The applied field causes the magnetization to cant out of the plane by an angle θ creating a demagnetizing field normal to the film but opposite the canting direction. 34

4.4 Domain wall mobility measurement using a nanowire with a width of 600 nm. The low field regime is linear up to the breakdown point of 4 Oe. A second linear regime occurs at higher fields. 42

4.5 Approximate magnetization structure of transverse (a) and vortex (b) domain walls calculated using micromagnetic simulations. Energy calculations of these two types of walls result in a phase boundary (c) for domain walls in Permalloy nanowires. 44

4.6 Mobility curves for nanowires of varying width. The high field mobility increases as the nanowire width increases. 45

4.7 The high field domain wall mobility for various widths of nanowires. The red line is a fit to a $\sqrt{w}$ function. The fit intersects the x-axis at ∼300 nm. 46

4.8 Domain wall mobility measurements under the influence of current. The zero current measurement is in black while the positive and negative current measurements are in blue and red, respectively. 51

4.9 Domain wall velocity as a function of current density at a driving field of 44 Oe (a) separated out into odd (b) and even (c) components. The odd component has a linear form while the even component is quadratic. 53

4.10 The odd (a) and even (b) components of velocity measurements for nanowires of various widths as a function of current. All measurements were conducted at a driving field of 45 Oe. The odd component is linear with the slope depending on width. The even component is quadratic and does not depend directly on width. 54

5.1 These measurements determine the injection delay time for a specific DC bias field. Each line represents a different field value. The period of the measurement waveform is varied and is used to determine the delay time for each point. The ratio of the signal Kerr amplitude to the reference Kerr amplitude then determines the probability that the domain wall is not injected. 60

5.2 The injection delay measurement for four wires of various widths was measured with time delays spanning nine decades. In the high slope region domain wall thermal activation dominates the injection mechanism. In the low slope region spin rotation dominates. 61

5.3 The injection delay measurements of Fig 5.2 are shifted horizontally such that the higher field region overlaps. The slope of the lower field region varies with nanowire width. 62

5.4 A large magnetic field first saturates both the nanowire and the continuous film. As the field is swept to the opposite polarity the continuous film switches first causing a domain wall to become pinned. When the field reaches the injection field the domain wall is injected into the nanowire. 66

5.5 The force from the pinning potential at the neck of the nanowire acts against the driving force from the external magnetic field. 67

5.6 The magnetization of the nanowire is monitored using Kerr measurements as the magnetic field is varied. These three resulting hysteresis loops were measured on three nanowires with different widths. The field at which the magnetization switches is the injection field. 67

5.7 The injection field shows an inverse relationship to the nanowire width. 69

6.1 A nanowire used to study a single domain wall requires the the nanowire be cut at one end to ensure that only a single domain wall traverses the nanowire. This nanowire is modified for electrical measurements with the addition of a Pt bridge using the GIS in the FIB. 71

6.2 The 300 kHz magnetic field waveform used to drive the domain wall for domain wall voltage measurements (a) is modulated by a 300 Hz, 10 Oe magnetic field. The driving field is shifted up during the positive polarity of the modulation field (b) and down for the negative polarity (c). 74

6.3 The expected form of the domain wall voltage measurement using a modulation technique. At points A and D the DC bias field is too large for domain walls to be continuously injected. When domain walls are continuously injected, the resulting voltage measured by the lock-in amplifier will be negative when the signal is out of phase with the modulation field (B) and positive when it is in phase with the modulation field (C). 75

6.4 The voltage induced by a moving domain wall measured with a modulation technique (a), is then separated into odd (b) and even (c) components for analysis. 77

6.5 A series of magnetic field waveforms with decreasing period is used to correlate the transit time of the domain wall with the measured voltage. 78

6.6 The domain wall voltage measured as the period of the driving magnetic field is decreased. The voltage reaches a peak at the wall transit time. Below the transit time the domain wall does not traverse the nanowire entirely causing a drop in the voltage measured, possibly due to multiple domain walls in the nanowire simultaneously moving in opposing directions. 79

6.7 A driving magnetic field with and without injection pulses. The dashed red line indicates the injection field level. The magnetic field without the injection pulse is below the injection field. No domain walls will be injected into the nanowire when this waveform is used. The addition of the injection pulse allows the domain wall to enter the nanowire. 80

6.8 Voltage measurements in the absence of a domain wall (black) and with a moving domain wall (red). The raw data (a) is separated into the odd (b) and even (c) components. The odd component (b) shows no voltage when a domain wall is not present in the nanowire (black). 82

6.9 The odd (a) and even (b) components of voltage measurements of a moving domain wall at various driving fields. The scaled voltage increases linearly with driving field (c). The voltage is scaled to compensate for the averaging of the lock-in amplifier. 84

Chapter 1

Introduction

Investigations of magnetic domain wall dynamics in nanostructures can provide useful information for understanding some of the fundamental questions in the physics of ferromagnetism. This understanding has been an area of interest recently as it will aid in the development of high performance magnetic devices. Experimental measurements of domains and domain dynamics have been conducted for a number of decades, however techniques to probe a single domain wall have been developed only recently. This thesis will describe a number of experiments that will further the understanding of magnetic domain wall dynamics.

1.0.1 Outline

This thesis is organized in the following manner. Chapter 2 will describe the basic concepts of magnetism, magnetic domain walls, and the magneto-optical Kerr effect. Chapter 3 will describe the experimental setup. This includes the fabrication of nanowires in Permalloy thin films using focused ion beam patterning and a description of a high spatial resolution magneto-optical Kerr effect polarimeter.

In Chapter 4, measurements of domain wall dynamics are presented along with variations due to the width of the nanostructures and the application of DC current. Chapter 5 presents the concept of a pinning potential at the interface between a nanowire and the continuous film of Permalloy along with the ability of a domain wall to overcome this potential. Chapter 6 presents the measurement of voltage induced by a moving domain wall. The final chapter will present overall conclusions as well as recommendations for future work.

Chapter 2

Background Theory

2.1 Ferromagnetism Basics

Ferromagnetism is a form of spontaneous magnetic ordering that can occur in a number of metallic elements and alloys. This phenomenon results from the interaction between electron spins known as the exchange interaction [1, 2, 3]. A model of magnetism based on the exchange interaction between local electrons was proposed by Heisenberg [1] with a Hamiltonian of the following form:

$$\hat{H} = -\sum_{i,j} J_{i,j} \hat{S}_i \cdot \hat{S}_j \tag{2.1}$$

Here the sum is taken over distinct pairs of spins, $\hat{S}_i$ and $\hat{S}_j$, at sites i and j. $J_{i,j}$ are the exchange constants representing the coupling between pairs of electrons. The ground state of the system is described as ferromagnetic when $J_{i,j}$ is positive. In this state all the spins are parallel and oriented in the same direction. The energy density associated with the exchange energy is given by:

$$E_{ex} = \frac{A}{M^2} |\nabla \vec{M}|^2 \tag{2.2}$$

where A is the exchange constant, a parameter of the material, and $\vec{M}$ is the magnetization, defined as the volume density of the net magnetic moment.

The exchange interaction is isotropic as it does not favor any particular direction. Experiments have shown, however, that ferromagnetic materials are generally anisotropic and are more easily magnetized in specific directions. This phenomenon is caused by a combination of the spin-orbit coupling and an external or demagnetizing field.

The spin-orbit coupling is the magnetostatic interaction between the intrinsic magnetic dipole moment of an electron and the magnetic dipole moment associated with the electron orbital motion. This interaction results in the magnetization favoring certain lattice directions in single crystals. This magnetocrystalline anisotropy energy density, E_{an}, can be generally written as

$$E_{an} = K \cdot f(\alpha_1, \alpha_2, \alpha_3) \tag{2.3}$$

Here K is the anisotropy constant, f depends on the spatial symmetry of the lattice, and $\alpha_1, \alpha_2, \alpha_3$ are the directional cosines of the magnetization with respect to the lattice primitive vectors. The directions for which $\vec{M}$ gives maxima and minima of E_{an} are respectively defined as the hard and easy axes. The simplest example is uniaxial anisotropy where $E_{an} = K\cos^2(\alpha)$. Magnetic anisotropy can also be induced by material growth conditions and physical size restrictions.

When an external magnetic field $\vec{H}$ is applied to a ferromagnetic material the energy density is given by

$$E_H = -\vec{H} \cdot \vec{M} \tag{2.4}$$

This energy is minimized when the magnetization is parallel to the applied field.

Even without an external magnetic field, a field known as the demagnetizing field exists. The demagnetizing field is the field each magnetic dipole sees as the result of being situated among all other dipoles in the material. The energy density associated with this demagnetizing field, $\vec{H}_{demag}$, is

$$E_{demag} = -\frac{1}{2}\vec{H}_{demag} \cdot \vec{M} \tag{2.5}$$

When the demagnetizing field extends beyond the physical borders of the material it is known as the stray field. The demagnetizing field of a uniformly magnetized ferromagnetic ellipsoid, for example, is given as

$$\mu_0 \vec{H}_{demag} = \mathbf{D} \cdot \vec{M} \tag{2.6}$$

Here $\mathbf{D}$ is the demagnetizing tensor with the diagonal components known as the demagnetizing factors. The directions with the lowest demagnetizing factors are the directions in which the material is most easily magnetized. In a thin film, approximated by an infinite plane, the demagnetizing factor in the plane $\mathbf{D}_{x,y} = 0$ while the demagnetizing factor perpendicular to the plane $\mathbf{D}_z = 1$. The preferred magnetization is then in the plane. For an infinite strip aligned with the x-axis, $\mathbf{D}_x = 0$, $\mathbf{D}_z \sim 1$, and $\mathbf{D}_y \ll \mathbf{D}_z$. The preferred magnetization will be along the axis of the strip.

The combination of these various interactions generally gives rise to an overall structure of the magnetization within a ferromagnetic material. Regions of uniform magnetization are called domains. Magnetic domains are

separated by narrow regions of rapidly changing magnetization known as domain walls. These structures will be discussed in more detail in the following section.

2.2 Magnetic Domain Walls

The formation of magnetic domains and domain walls in a ferromagnetic material is a result of the minimization of the energies associated with the exchange interaction, the anisotropy, the demagnetizing field, and external fields. For instance, in thin films of magnetic material it has been shown [4] that a magnetic configuration with minimal stray fields is only possible with the introduction of domain walls.

A single domain structure will produce large stray fields as shown in Fig 2.1a. In order to minimize the energy created by the stray fields, the formation of closure domains is energetically favorable in most cases. A classic closure domain structure is shown in Fig 2.1b. The increase in energy resulting from the exchange energy and anisotropy energy are generally much smaller than the decrease that results from minimizing the stray fields.

Domain walls are classified into two types, Bloch and Néel. In a Bloch wall, the magnetization in the domain wall rotates out of the plane created by the magnetization on either side. Néel domain walls, which generally are present in magnetic thin films, consist of rotation that remains in the primary plane of magnetization. Examples of 180° Bloch and Néel domain walls are shown in Fig 2.2a. The magnetization in each wall rotates continuously from

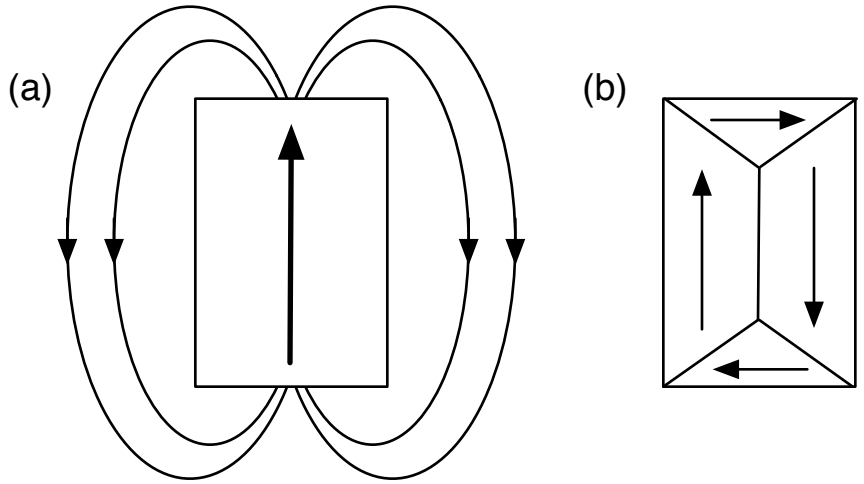

Figure 2.1: A single domain structure (a) will have large stray fields. The stray fields are minimized by the formation of closure domains (b).

one side of the domain wall to the other. The edges of the domain wall are indicated by the dotted red lines.

In a thin strip of magnetic material, the magnetization will align along the length of the strip. When a 180° Néel wall is introduced into the strip, the direction of the magnetization on either side of the domain wall is described as either a head-to-head or a tail-to-tail configuration, as shown in Fig 2.2b.

In the absence of external fields, the distribution of spin angles ϕ within a domain wall can be calculated by minimizing the sum of the exchange energy and the anisotropy energy [1]. Here the exchange energy is given as $E_{ex} = A(\frac{\partial \phi}{\partial x})^2$, from Eq (2.2), and with a uniaxial anisotropy the anisotropy energy is given as $E_{an} = K\cos^2(\alpha)$. Using a minimization technique, the resulting

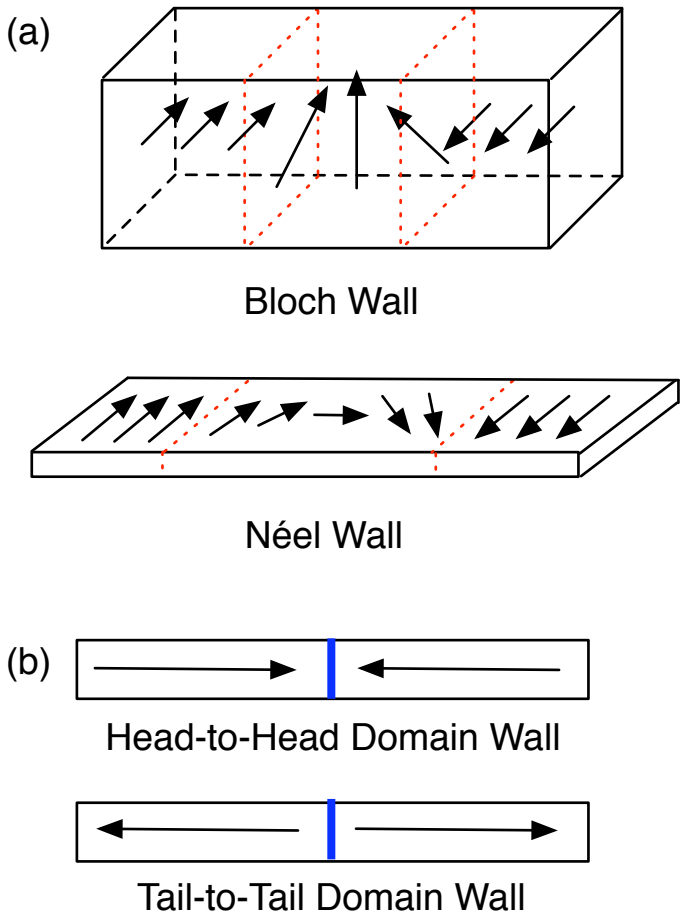

Figure 2.2: The two types of domain walls (a), Bloch and Néel. The red dotted lines represent the edges of the domain walls. Néel walls are generally present in thin films. In a strip of magnetic thin film (b) Néel domain walls, represented by the blue line, will generally form either a head-to-head or a tail-to-tail domain wall.

spin angle distribution is given as

$$x(\phi) = \sqrt{\frac{A}{K}} \ln\left(\tan\left(\frac{\phi}{2} + \frac{\pi}{4}\right)\right) \tag{2.7}$$

From this equation, the domain wall width would appear to be infinite. An effective domain wall width is conventionally defined as the length of a wall in which the spin rotation at the center of the wall remains constant over the length of the wall. The domain wall width then becomes

$$\Delta = \pi\left(\frac{\partial x}{\partial \phi}\right)_{x=0} = \pi\sqrt{\frac{A}{K}} \tag{2.8}$$

The spin angle distribution of Eq (2.7) is shown in Fig 2.3. The dotted line represents the effective domain wall width of Eq (2.8).

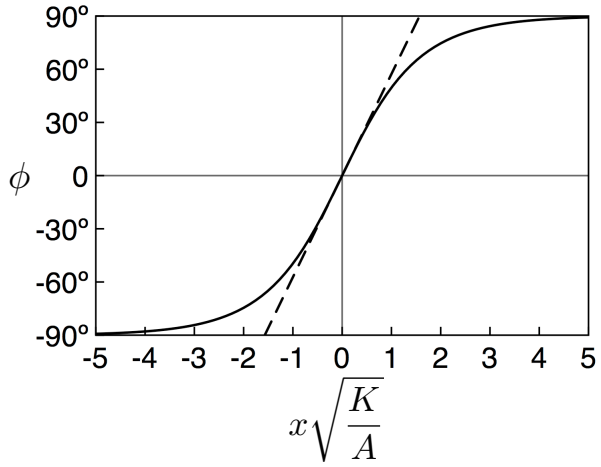

Figure 2.3: The spin angle distribution in a domain wall in a material with uniaxial anisotropy. The dotted line represents the effective domain wall width.

2.3 Magnetic Domain Wall Dynamics

A single magnetic dipole moment $\vec{M}$ placed in a magnetic field $\vec{H}$ rotates around the field axis with a rate proportional to the field torque:

$$\frac{d\vec{M}}{dt} = -\gamma \vec{M} \times \vec{H} \tag{2.9}$$

where γ is the electron gyromagnetic ratio. In order to adapt Eq (2.9) to describe the dynamics of the magnetization $\vec{M}$ inside a ferromagnet $\vec{H}$ is assumed to be the effective field (the combination of the external, exchange, and demagnetizing fields) and a damping term must be added to describe the magnetization relaxation towards the effective field axis:

$$\frac{d\vec{M}}{dt} = -\gamma \vec{M} \times \vec{H} + \alpha\gamma \frac{\vec{M} \times (\vec{M} \times \vec{H})}{M} \tag{2.10}$$

Here α is the damping parameter. Eq (2.10) was originally proposed by Landau and Lifshitz [5]. Another version of this equation was proposed by Gilbert [6] who replaced the field torque part of the damping term with the time derivative of the magnetization $\frac{d\vec{M}}{dt}$:

$$\frac{d\vec{M}}{dt} = -\gamma \vec{M} \times \vec{H} + \alpha \frac{\vec{M} \times \frac{d\vec{M}}{dt}}{M} \tag{2.11}$$

Eq (2.11) is known as the Landau-Lifshitz-Gilbert (LLG) equation. Eqs (2.10) and (2.11) are equivalent when the damping constant is small ($\alpha \ll 1$).

The magnetization can be phenomenologically approximated as a physical vector in a viscous medium. From this approximation a relationship between the field magnitude and the domain wall velocity can be derived. We

start with a head-to-head domain wall and apply a magnetic field in the $+x$ direction. In order to lower the magnetostatic energy, the domain wall will move in the $+x$ direction. The magnetization will initially be in the $-x$ direction and will rotate from $-x$ to $+x$ as the domain wall moves. In doing so, the magnetostatic energy in a volume V is changed by the amount $-2MHV$. This energy is dissipated through the torque on the viscous medium, $-A(\frac{d\phi}{dt})V$, as it rotates from $\phi = 0$ to $\phi = \pi$.

$$2MHV = \int_0^\pi A\left(\frac{d\phi}{dt}\right)V d\phi \tag{2.12}$$

Here A is a viscous damping constant and $\frac{d\phi}{dt}$ is the angular velocity of the vector. We can relate angular velocity to the domain wall velocity, $v = \frac{dx}{dt}$.

$$\frac{d\phi}{dt} = \frac{dx}{dt}\frac{d\phi}{dx} = v\frac{d\phi}{dx} \tag{2.13}$$

Plugging Eq (2.13) back into Eq (2.12) gives us the domain wall velocity as a function of the applied field, H

$$v = \frac{2MH}{A \cdot \int_0^\pi (\frac{d\phi}{dx})V d\phi} = \mu H \tag{2.14}$$

where μ is the domain wall mobility.

2.4 The Magneto-optical Kerr Effect

The magneto-optical Kerr effect (MOKE) is a simple way to study the magnetization in thin films with a reflective surface. The effect occurs when linearly polarized light is reflected off of a magnetic material. The magnetization of the surface causes characteristics of the reflected beam to be changed

by a small amount. These changes can be measured and used to determine information about the magnetization state of the material.

While a full microscopic view of MOKE involves the interaction between the spin polarization and the quantum-mechanical spin-orbit coupling [7], here it will be described by a classical interaction between the polarized incident light and the electrons at the surface of the reflecting material. The polarized beam will cause these electrons to oscillate along the electric field direction. The magnetization of the sample, $\vec{M}$, causes the oscillating electrons to experience the Lorentz force, $\vec{F}_L = \vec{E} \times \vec{M}$. The Lorentz force induces a secondary motion in the electrons perpendicular to the electric field. This secondary motion adds a component to the electric field causing the polarization of the reflected beam to be rotated relative to the incident plane of polarization. The rotation of the reflected beam can be measured by using analyzing polarizers to measure the scalar components of the polarization vector.

There are three distinct geometries for MOKE measurements depending on the orientation of the magnetization of the material being measured [8, 9] as shown in Fig 2.4. In the polar configuration, the magnetization is normal to the surface. The polar effect rotates the plane of polarization of the reflected beam and is strongest when the incident beam is perpendicular to the surface. In the transverse configuration, the magnetization is parallel to the surface and perpendicular to the plane of incidence. The transverse effect does not rotate the polarization, but if the beam is polarized in the plane of incidence the reflected intensity will depend on the magnetization. In the

longitudinal configuration, the magnetization is parallel to the surface and parallel to the plane of incidence. The longitudinal effect rotates the polarization with an angle that is proportional to the magnetization.

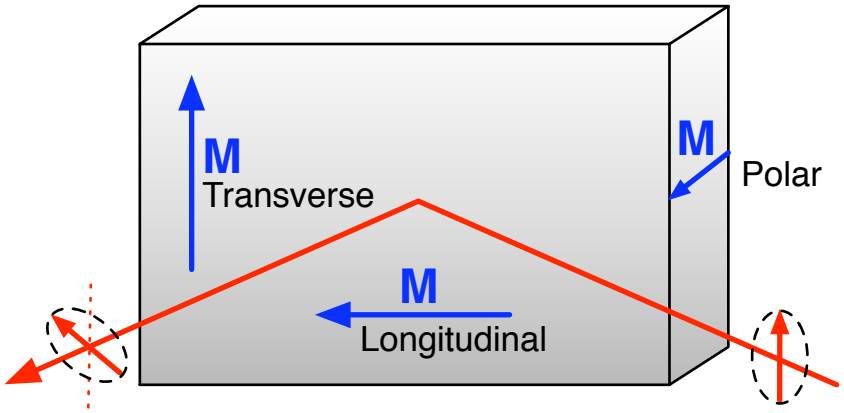

Figure 2.4: The three MOKE geometries describe the relative orientation between the magnetization of the material and the polarized light source. The three geometries are polar, transverse, and longitudinal. The rotation of the polarization of the light source, in this case a polarized laser indicated by the red line in a plane perpendicular to the material, depends on the magnetization of the material.

Chapter 3

Experimental Setup

3.1 Device Fabrication via Focused Ion Beam Patterning

Each device used in the experiments described in this thesis was fabricated from a thin film of permalloy (Py), an alloy of nickel and iron ($Ni_{80}Fe_{20}$). The permalloy film was grown with tantalum capping layers into a structure of Ta(3 nm)/Py(20 nm)/Ta(5 nm) on a 125 μm thick substrate of thermally oxidized Si(100) using DC magnetron sputtering at room temperature. Structures were then created in the continuous film by removing material using a focused ion beam (FIB). The FIB system (FEI Strata DB235) removes surface atoms by bombarding them with a focused beam of highly energetic Ga^+ ions. This system can create patterns with a spatial resolution of ~ 5 nm.

The structures used in this thesis are referred to as nanowires as the width of the narrowest is on the order of a few hundred nanometers and the length is much larger than the width ($L \gg w$). Permalloy is removed via FIB from two rectangular shaped areas at least 35 μm in length, 6 μm wide, and separated by a distance that defines the width w of the nanowire. The resulting structure is a nanowire of width w connected at both ends to the continuous film of permalloy. For all nanowires, the ion beam accelerating

voltage was set to 30 kV and the aperture was set to limit the beam current to 100 pA.

Material is removed from these rectangles using two raster modes. A schematic layout of the material removed is shown in Fig 3.1. The majority of the material is removed in the normal mode where the ion beam scans through the entire rectangle. This causes the area to reach a fraction of the intended depth. After each additional scan of the area, the rectangle increases in depth until it reaches its final depth.

The final amount of material is removed from the edge of the nanowire in what is called the "cleaning cross section" mode. In this mode the ion beam removes a single line at a time to the intended depth. The initial line is made adjacent to the previously removed rectangular area. The ion beam then removes subsequent lines increasing the size of the rectangular area of removed material until the intended width is achieved. The final line of material removed becomes the edge of the nanowire. This method allows for a much cleaner edge to the nanowire than if the entire area was removed in the normal raster mode.

A single domain wall can be studied by removing material from one end of the wire, disconnecting it from the continuous film, and creating a point in the resulting nanowire end. The point discourages domain walls from nucleating at the end of the nanowire. Domain walls then only enter the nanowire from the continuous film. An example of this type of nanowire is shown in Fig 3.2. A discussion of the dynamics of a single domain wall in this

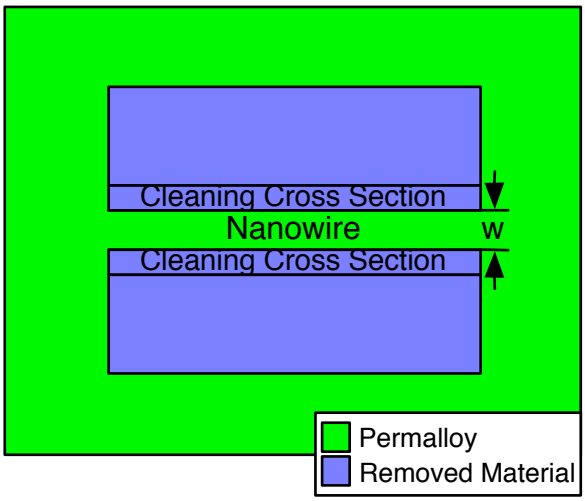

Figure 3.1: A schematic of material removed from the continuous permalloy film resulting in a nanowire of width w. The larger rectangular areas are removed using the normal raster mode. The areas along the nanowire edges are removed via the cleaning cross section mode with the final line of material removed forming the edge of the nanowire.

configuration can be found in Section 4.2.

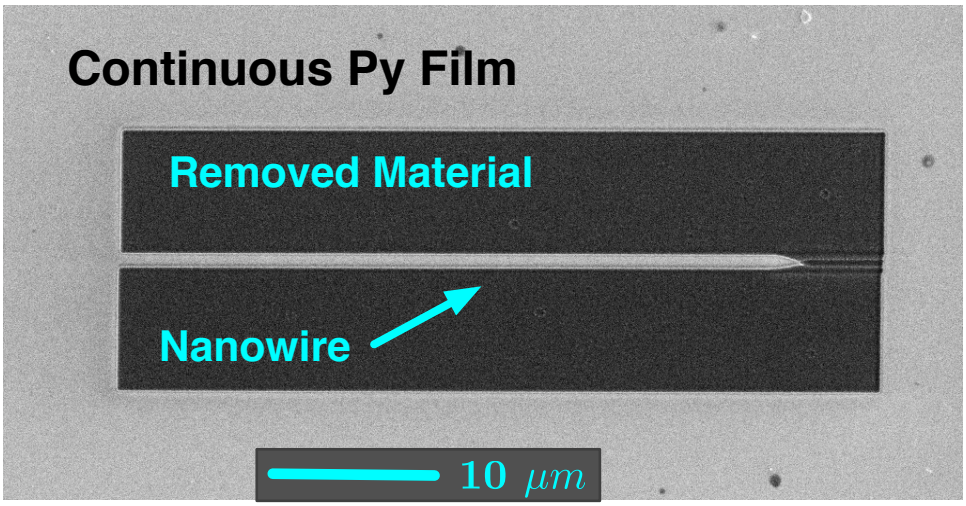

Figure 3.2: An example of a nanowire with one end cut created by removing material from a permalloy film using a focused ion beam. This configuration is used to study a single domain wall.

If both ends of the nanowire remain connected, two domain walls of opposite orientation (one head-to-head and one tail-to-tail) can be observed. One domain wall will enter the nanowire from each end and move towards the center. An example of this type of nanowire is shown in Fig 3.3. This configuration can be used to study the influence of electric current on the motion of the domain walls if one end of the nanowire is electrically isolated from the other end. This is accomplished by creating a contact pad in the continuous film on one side of the nanowire as shown in Fig 3.4. Measurements in this configuration are discussed in further detail in Section 4.4.

The FIB fabrication process is versatile enough to make nanowires of

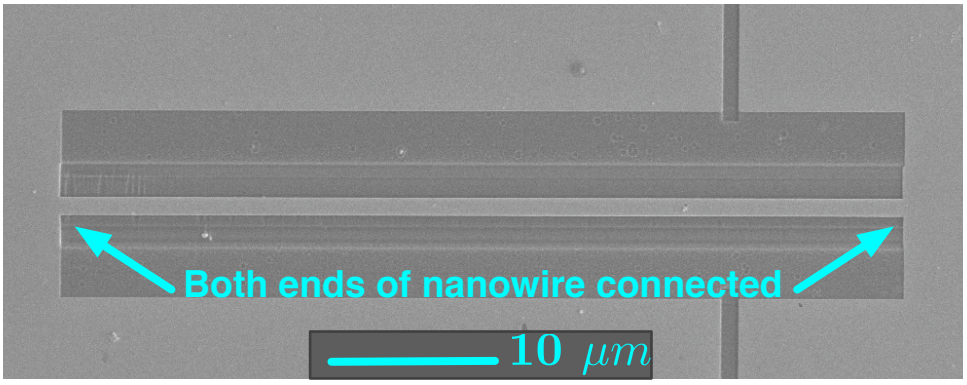

Figure 3.3: A nanowire with both ends connected created by removing material from a permalloy film using a focused ion beam. This configuration can be used to study domain wall dynamics under the influence of current by electrically isolating one end of the nanowire from the other.

any width necessary. Nanowires of widths from 200 nm to 3 μm have been studied. A detailed analysis of the effects of this width variation is presented in Section 4.3

In addition to the removal of material, the FIB system has a gas injection system (GIS) that can deposit platinum. The system uses an organometallic compound with Pt at the center. This compound is evaporated through a pinhole into the FIB system chamber. The gas interacts with the ion beam causing the Pt to be released from the molecule onto the sample. Patterns are formed in the same manner as the patterns for the removal of material. This function allows non-magnetic metal, Pt in this case, to be deposited on the permalloy structures to be used in electrical measurements.

The FIB system is also equipped with a nanomanipulator (Zyvex S100).

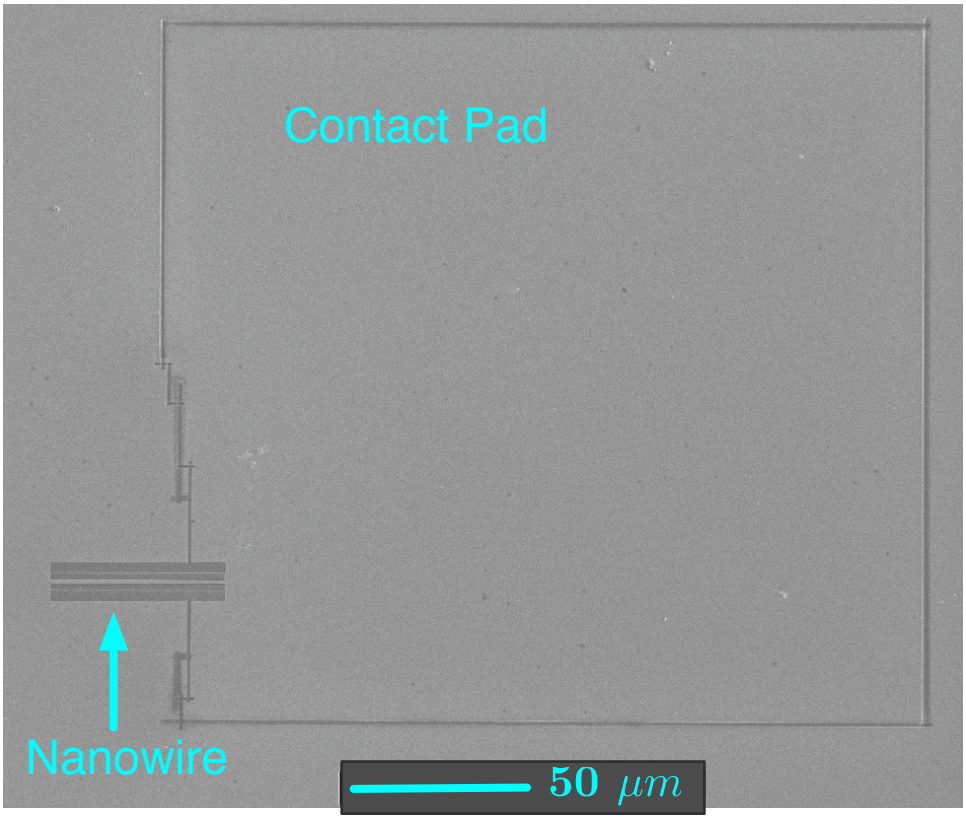

Figure 3.4: A contact pad made with FIB in a permalloy film. The dimensions of this contact pad are of sufficient size to allow a wire bond contact to be applied for current measurements.

This consists of four miniature XYZ stages that can be mounted around the sample stage inside the FIB system. Each stage has a 12 mm range in each direction. A piezoelectric tube is mounted on each stage for fine position adjustments. A sharp, rigid probe is then attached to the end of each piezoelectric tube. Each probe has an electrical connection to outside the FIB system so that the probes can be used for various measurements. For the purposes of these experiments, the probes were used for *in situ* resistance measurements of nanowires. Since there are 4 probes, resistance can be measured in either the two or four probe configurations. Fig 3.5 shows the tips of the probes in a four probe resistance measurement configuration.

3.2 Magnetization Measurements with a MOKE Polarimeter

Domain wall dynamics can be probed using the magneto-optical Kerr effect, or MOKE, described in Section 2.4. This section will describe the MOKE polarimeter used to measure the domain wall dynamics described in the following chapters. This custom built polarimeter can make measurements with a spatial resolution of $\sim 1\,\mu m$ and a temporal resolution of less than 2 ns [10]. A diagram showing the schematic setup of the MOKE polarimeter is presented in Figure 3.6.

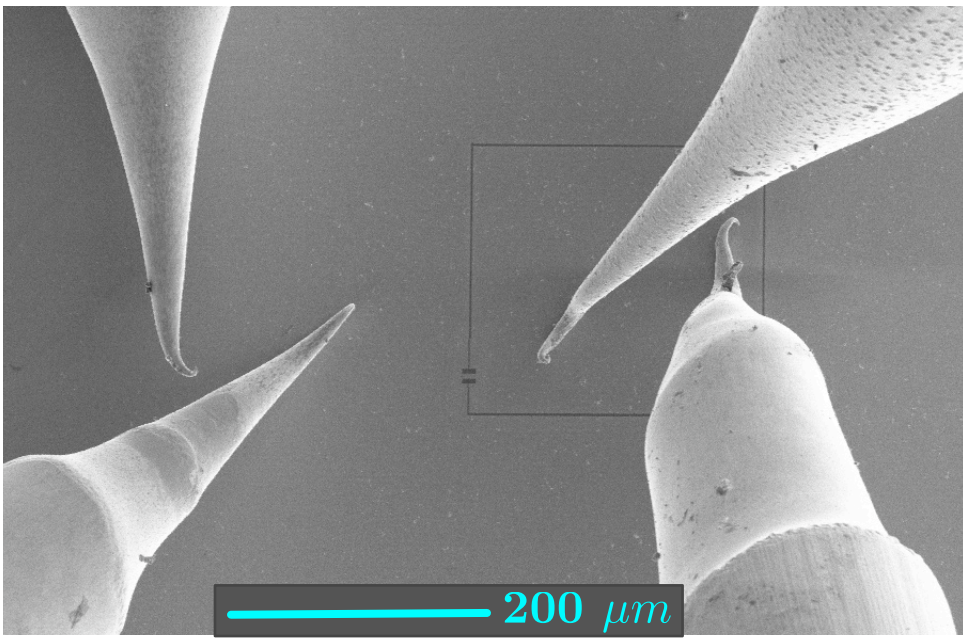

Figure 3.5: Nanomanipulator probes inside the FIB chamber allow for *in situ* electrical measurements. Here the probes are configured for a four probe resistance measurement.

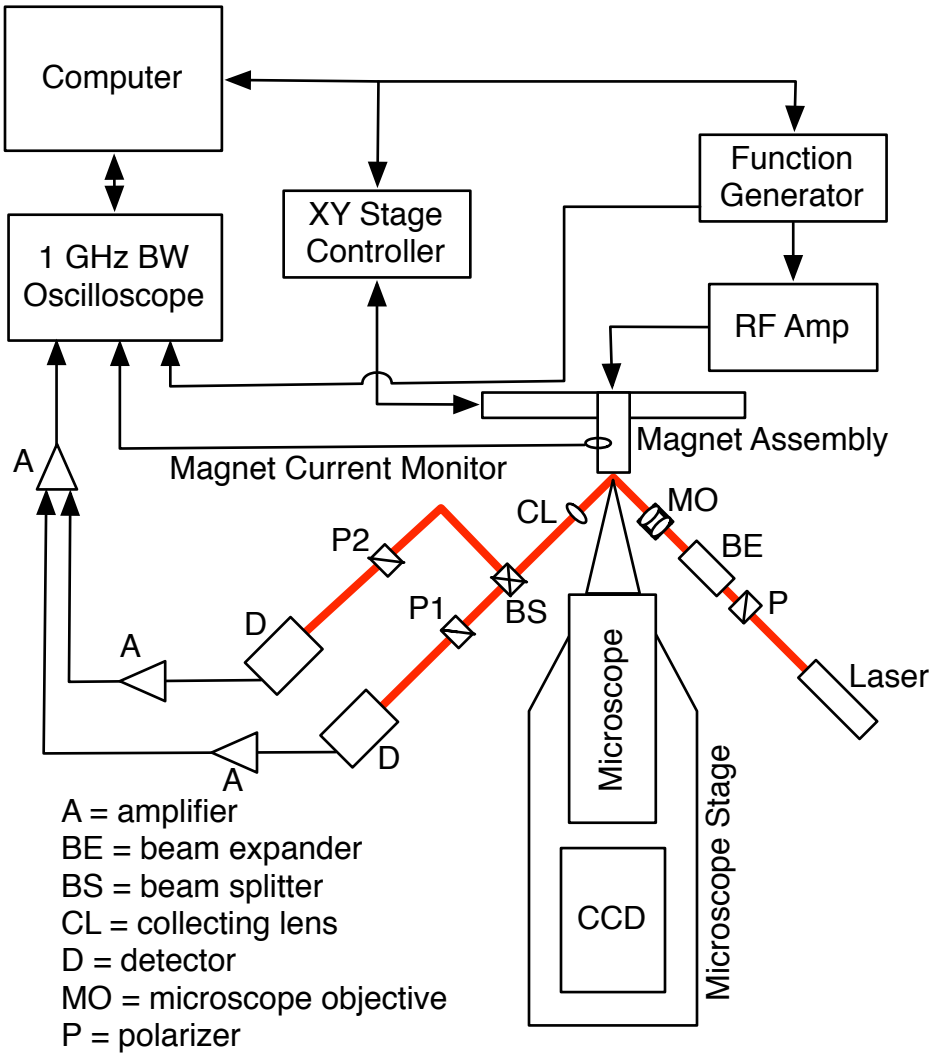

Figure 3.6: A schematic of the components for the MOKE polarimeter.

3.2.1 Polarimeter Optics and Signal Acquisition

The light source for the polarimeter is a solid state laser (CrystaLaser RCL-658-50) with an operating wavelength of 658 nm and a maximum power output of 50 mW. The beam is polarized by a Glan-Taylor prism polarizer before being sent through a $\times 20$ beam expander. This expands the beam to the size of the focusing lens, a $\times 10$ microscope objective with a 0.28 numerical aperture. The microscope objective is mounted on a commercial 3-axis manual flexure stage with on axis aligned with the beam. This allows the size of the focused laser beam on the sample to be adjusted. The beam is then incident at 45° to the sample. The reflected light is then collected by a 25 mm diameter convex lens with a $\sim$0.33 numerical aperture to approximately match the microscope objective. This matching is to ensure that all of the light from the reflected beam is collected.

Since the signal from the MOKE rotation is small, a differential method of detection is used to minimize unwanted signals. A 50/50 non-polarizing beam splitter divides the reflected beam into two equal sub-beams. These beams are sent to two Glan-Taylor polarizers at polarizing angles of $+\alpha$ and $-\alpha$. The differential signal is the difference between the two transmitted intensities. This method also removes noise from fluctuations in beam intensity and any mechanical vibrations of the various optical surfaces.

For the high-bandwidth measurements taken in these experiments, fast photomultiplier tubes (PMT) (Hamamatsu R1894) were used for photodetection. The output for each PMT is amplified by two Stanford Research Systems

SIM914 pre-amplifiers. Each pre-amplifier has a $\times 5$ gain, a 350 MHz bandwidth, and is DC coupled. The amplified signals are then subtracted by a 500 MHz differential amplifier probe (LeCroy AP033) that sends the difference signal to an 8-bit, 1 GHz-bandwidth digital oscilloscope (LeCroy WavePro 960).

The polarimeter is equipped with a microscope to aid in the alignment of structures relative to the magnet system and of the laser relative to the structures. This microscope consists of a CCD camera (Princeton Research Pentamax) that feeds images to a computer and a long focal length reflecting microscope (Questar QM-100). On-axis illumination of the sample is accomplished by placing a prism inside the microscope and illuminating it with a 150 W tungsten fiber-optic light source.

3.2.2 Polarimeter Magnet System

The magnet system used to drive domain walls in each device is custom built for high-bandwidth measurements. The magnet system is based on a step-down ferrite-core transformer with a 4:1 turns ratio. Magnetic fields are created by passing current through a 4 mm long, 500 μm wide copper wire on the secondary winding of the transformer. This magnet wire has a semicircular cross section and is soldered between two 1/4 inch thick copper electrodes. The magnet system can generate currents up to 15 A at frequencies from DC to $\sim$20 MHz.

The semicircular wire produces an axial magnetic field. When a 125

μm thick substrate is placed on the flat side of the wire, the in-plane field at the surface of the substrate has a value of $\sim$5 Oe/A. The field is uniform to within 5% over a distance of at least 200 μm in the plane of the substrate and perpendicular to the wire.

In order to measure the magnetic field produced by the wire, the current is monitored using a 200 MHz passive inductive current monitor (Pearson model 2878) on the secondary coil side of the transformer. This current monitor is electrically insulated from the magnet system and can measure current peaks up to 100 A. The primary input of the magnet system is driven by a solid-state amplifier (Amplifier Research 150A-100B) with a 10 kHz - 100 MHz bandwidth and 150 W maximum output. This is in turn driven by a signal generator (Standford Research Systems DS345) with a DC - 30 MHz bandwidth.

The magnet system is mounted on a two-axis translation stage (Daedal 800,000 series) that is mounted vertically on the optical table. When the sample is mounted to the magnet, this allows the sample to move relative to the position of the laser spot while remaining fixed in relation to the magnet. The stepper motors that move the translation stage have a step size of $\sim$20 nm.

In addition to the high frequency magnet, the system also includes a single Helmholtz coil magnet. This magnet can be used to provide a DC bias field to a sample mounted on the high frequency magnet.

The operation of the polarimeter is computer controlled using software written in LabVIEW. The digital oscilloscope and signal generator are controlled over an IEEE bus. The translation stage for the sample and magnet system are controlled using a RS232 bus. The software includes functions that will scan the sample with the translation stage while collecting MOKE data at each point as well as custom magnet waveform design using the arbitrary waveform function of the signal generator.

Chapter 4

Domain Wall Dynamics

The discovery of giant magnetoresistance (GMR) in 1988 [11, 12] was the impetus that led to the development of electronic devices that utilized the spin state of electrons to a large degree. This new technology is referred to as magnetoelectronics or, more commonly, spintronics [13]. The concepts of GMR were quickly developed into read heads for hard disk drives [14, 15, 16], allowing for the sharp increase to the density of information storage seen in computers and other devices today. Another spintronic device already in production is magnetic random access memory (MRAM) that uses the concept of tunneling magnetoresistance (TMR) in the form of magnetic tunnel junctions (MTJ) [17, 18, 19].

Other devices have been suggested that utilize the manipulation of magnetic domain walls. Memory [20, 21] and logic devices [22, 23, 24] with domain walls acting as information carriers have been proposed with the possibility of moving the domain walls with either magnetic field or current [25]. In order to determine the feasibility of these devices, detailed models and experimental measurements must be developed. One important characteristic of domain walls is the mobility, or the change in velocity with a change in

external magnetic field or applied current. This chapter will describe the first mobility measurements conducted on a single domain wall [26] followed by expansions on this measurement by varying the width of the nanowire and applying current through the nanowire.

4.1 Measurement Methods

In order to measure and study the dynamics of magnetic domain walls, nanowires are fabricated out of a thin film of permalloy using a focused ion beam (FIB) as described in Section 3.1.

The nanowire structure is mounted onto the MOKE polarimeter using a circular macor piece to hold the substrate against the semi-circular magnet wire. The nanowire alignment is verified with the aid of the polarimeter microscope. The nanowire must be aligned such that the magnetic field resulting from the current in the magnet wire is parallel to the nanowire. The microscope is also used to ensure that the nanowire is located as close to the center of the magnet wire as possible.

In this configuration the magnetization of the nanowire will be in the plane of incidence of the polarimeter laser beam. The polarimeter is setup to measure changes in the longitudinal component of the magnetization by choosing the beam polarization to be perpendicular to the plane of incidence ("s" polarization). The reflected beam carries the Kerr signal induced by the nanowire magnetization. The magnitude of this signal is proportional to the fraction of the beam that is reflected off of the wire. Therefore it is necessary

to have the beam centered on the nanowire and for the beam to have the smallest possible diameter.

The beam size is measured by scanning the beam across a cleaved edge of the substrate and measuring the reflectivity. The resulting intensity profile is fitted with an error function and the differential profile is fitted with a Gaussian whose width represents the beam diameter along the scanning direction. The beam diameter can be adjusted by moving the microscope objective along the laser beam with the flexure stage on which the objective is mounted.

Once the beam size is properly adjusted, the beam is approximately aligned with the nanowire using the polarimeter microscope. The exact coordinates of the nanowire are then determined by creating a susceptibility map of the area. This is accomplished by applying a 10 kHz bipolar square wave to the magnet wire with an amplitude that will saturate the nanowire in both directions. The Kerr signal is measured by a lock-in amplifier locked to the frequency of the square wave. A two dimensional scan of the magnetic susceptibility of a nanowire compared to a SEM image of the same wire is show in Figure 4.1.

Once the beam is centered on the nanowire, the velocity of a domain wall traveling through the wire can be measured. This is accomplished by applying a cyclic magnetic field waveform to the nanowire and measuring the Kerr signal at equally spaced points along the nanowire. The waveforms consist of a large pulse that will saturate the nanowire in one direction followed by a second pulse in the opposite direction. The second pulse is adjusted such

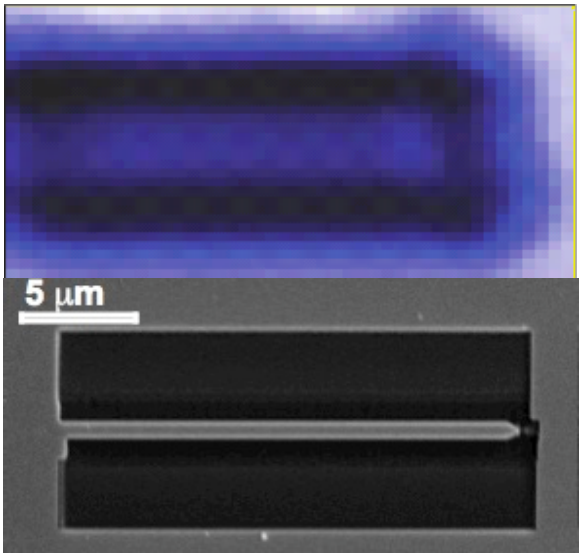

Figure 4.1: The magnetic susceptibility and SEM images of a nanowire. The susceptibility signal is the result of a lock-in amplifier measuring the MOKE signal at the frequency of a saturating square wave magnetic field. The darkest coloration in the susceptibility image represents a lack of MOKE signal.

that it creates a constant magnetic field during the entire transit time of the domain wall through the nanowire. During each cycle of the waveform, the magnetization of the extended film will switch directions before the magnetization of the nanowire due to the shape anisotropy of the nanowire. This causes a domain wall to become trapped, or pinned, at the boundary between the nanowire and the continuous film. The domain wall is then "injected" into the nanowire and propagates along the nanowire. The mechanics of this injection are discussed in more detail in Chapter 5.

Figure 4.2 shows examples of Kerr signal transients resulting from the domain wall passing through the focused laser spot at subsequent points along the nanowire. The Kerr signal transients are averaged over at least 40,000 cycles in order to improve the signal to noise ratio. These transients show that the further from the domain wall injection point the Kerr signal is measured, the later the delay in the magnetization reversal of the nanowire. This indicates that the nanowire reverses its magnetization through the motion of a single domain wall moving from the continuous film along the length of the nanowire.

Each transient is fitted with an error function and the center of the error function defines the time of reversal. The velocity of the domain wall can then be calculated from the position of the laser beam along the nanowire and the time delay of magnetization reversal. This velocity measurement method is used to study the behavior of the domain wall while varying the driving magnetic field (Sec. 4.2), varying the width of the nanowire (Sec. 4.3), and applying a DC current (Sec. 4.4).

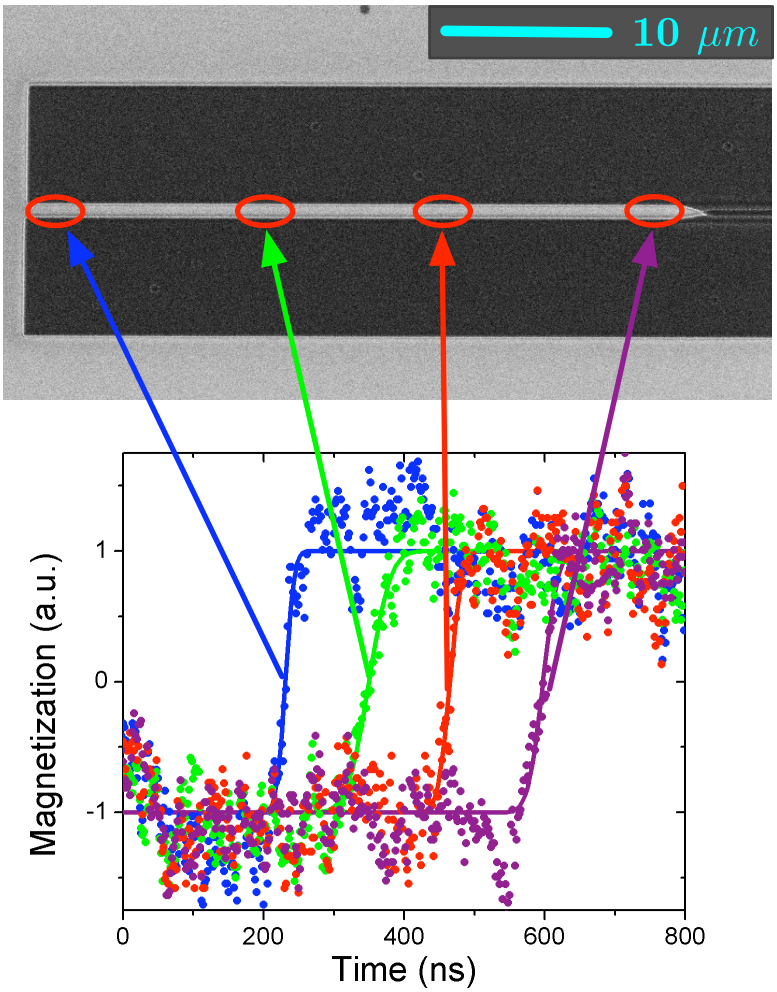

Figure 4.2: Kerr signal transients measured along a nanowire. As the laser spot moves along the nanowire the time of reversal increases. The position and reversal time data is then used to calculate the domain wall velocity.

4.2 Field Driven Domain Wall Dynamics

In order to characterize the motion of a magnetic domain wall, the mobility of the domain wall is measured. The mobility is defined as rate of change of the velocity of the domain wall with increasing applied magnetic field. This section presents the simplest model of domain wall mobility and experimental measurements of the domain wall velocity over a broad range of applied magnetic fields.

4.2.1 Model for Domain Wall Motion

The basic model that is used to describe the behavior observed in the velocity measurements begins with a static domain wall placed in a single line of spins. Permalloy films will have Néel type domain walls below a film thickness of 30 nm [27, 28]. Néel walls are energetically favorable due to the large out-of-plane demagnetizing factor at these thicknesses. Since the films used for these measurements are 20 nm, we assume the domain walls to be Néel type.

We start with a domain wall with zero external field and then apply a field $\vec{H}_a$ along the axis of the nanowire, as seen in Fig 4.3. According to the LLG equation there will be a torque $\vec{M} \times \vec{H}_a$ normal to the sample plane. This causes the magnetic moments to cant out of the sample plane, introducing a demagnetizing field in the opposite direction as the out of plane component of $\vec{M}$. The demagnetizing field exerts a torque $\vec{M} \times \vec{H}_{dem}$ causing the magnetic moments to precess around the sample normal. This precession is equivalent

to motion of the domain wall along the nanowire.

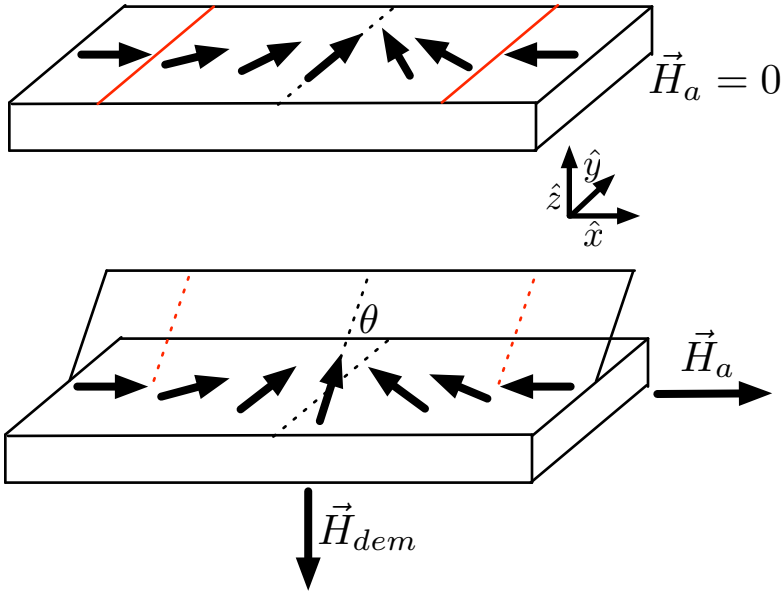

Figure 4.3: The configuration of the magnetization in a Néel domain wall at zero applied field and with a non-zero applied field. The red lines represent the edges of the domain wall. The applied field causes the magnetization to cant out of the plane by an angle θ creating a demagnetizing field normal to the film but opposite the canting direction.

In order to get a more quantitative version of this model, two approximations must be made about the domain wall. The first is that domain wall is a transverse wall that is symmetric and that the canting angle θ is small ($\theta \ll 90°$). To a first approximation, small angle wall canting does not significantly change the effective anisotropy constant K_{eff} in the wall width formula

$$\Delta = \pi \sqrt{\frac{A}{K_{eff}}} \tag{4.1}$$

where $K_{eff} = K + 2\pi D M_s^2$. K is the anisotropy energy density of the continuous film and D is the nanowire demagnetizing factor. In this case, D is much larger than K, so K can be neglected.

The second approximation is that the domain wall is rigid. Although it cants it does not change its configuration or width. The domain wall changes angle by 180° from one side of the wall to the other. Since the canting angle produced during the domain wall motion is much smaller than 180°, the exchange energy will not change significantly from the static domain wall case. Since both the anisotropy and exchange energy do not change, the domain wall is considered rigid with a wall width of Δ.

The starting point for describing the dynamics of the domain wall is the LLG formula

$$\frac{d\vec{M}}{dt} = -\gamma \vec{M} \times \vec{H}_{eff} + \alpha \frac{\vec{M} \times \frac{d\vec{M}}{dt}}{M} \tag{4.2}$$

where $\vec{H}_{eff}$ is the effective field and $\vec{M}$ is the magnetic moment of the wall. When an external field is applied along the nanowire the domain wall will move with a velocity v and cant at an angle θ. The demagnetizing field caused by the canting of the wall is

$$\vec{H}_{dem} = -D_z M \sin(\theta)\hat{z} - D_y M \cos(\theta)\hat{y} \tag{4.3}$$

where $\hat{x}$ is along the wire in the direction of motion of the domain wall, $\hat{y}$ is perpendicular to the wire in the sample plane, and $\hat{z}$ is normal to the sample plane. D_z and D_y are the demagnetizing factors in the z and y direction, respectively. In this case, $D_z \sim 1$ and $D_y \ll D_z$ so the component in the y

direction can be neglected [29]. The effective field, which is the sum of the applied field $\vec{H}_a$ and the demagnetizing field $\vec{H}_{dem}$ then becomes

$$\vec{H}_{eff} = \vec{H}_a - M \sin\theta \hat{z} \tag{4.4}$$

We can then use $\vec{H}_{eff}$ so that the first term of the right-hand side of Eq (4.2) becomes

$$\begin{aligned} -\gamma \vec{M} \times \vec{H}_{eff} = (-\gamma) M^2 \sin\theta \cos\theta \hat{x} \\ + (-\gamma)(-M H_a \sin\theta)\hat{y} + (-\gamma)(-M H_a \cos\theta)\hat{z} \end{aligned} \tag{4.5}$$

The left-hand side of Eq (4.2) can be expressed as

$$\frac{d\vec{M}}{dt} = \frac{\partial \vec{M}}{\partial \vec{r}} \frac{\partial \vec{r}}{\partial t} \tag{4.6}$$

$\frac{\partial \vec{M}}{\partial \vec{r}}$ is the spatial rate of change of the magnetization at the center of the domain wall. For a typical Néel wall, the longitudinal component of the magnetization is

$$M_x = M \tanh(\frac{x}{\Delta}) \tag{4.7}$$

where $x = 0$ is at the center of the wall [30]. Taking the derivative of this gives

$$\frac{\partial \vec{M}}{\partial \vec{r}} = \frac{dM_x}{dx} = \frac{d(M \tanh(\frac{x}{\Delta}))}{dx} = \frac{M}{\Delta}(1 - \tanh^2(\frac{x}{\Delta})) \tag{4.8}$$

When evaluated at $x = 0$ and setting $\frac{\partial \vec{r}}{\partial t} = \vec{v}$, this results in

$$\frac{d\vec{M}}{dt} = \frac{M}{\Delta} v \hat{x} \tag{4.9}$$

By expressing the canting terms of the magnetization as

$$\vec{M} = M \sin(\theta)\hat{z} + M \cos(\theta)\hat{y} \tag{4.10}$$

and using the resutls of Eq (4.9), the second term of the right-hand side of Eq (4.2) becomes

$$\alpha \frac{\vec{M} \times \frac{d\vec{M}}{dt}}{M} = \frac{\alpha M}{\Delta} v \sin\theta \hat{y} + \frac{\alpha M}{\Delta} v \cos\theta \hat{z} \tag{4.11}$$

We then combine Eqs (4.5), (4.9), and (4.11) into Eq (4.2) and separate out the scalar components of the three basis directions into

$$\hat{x} : \frac{M}{\Delta} v = -\gamma M^2 \sin\theta \cos\theta \tag{4.12}$$

$$\hat{y} : 0 = \gamma M H_a \sin\theta + \frac{\alpha M}{\Delta} v \sin\theta \tag{4.13}$$

$$\hat{z} : 0 = \gamma M H_a \cos\theta + \frac{\alpha M}{\Delta} v \cos\theta \tag{4.14}$$

These three equations can be used to solve for the canting angle θ and the domain wall velocity v resulting in

$$\sin 2\theta = -\frac{2H_a}{\alpha M} \tag{4.15}$$

and

$$v = \frac{\gamma \Delta}{\alpha} H_a = \mu H_a \tag{4.16}$$

where μ is the domain wall mobility. The domain wall velocity is therefore proportional to the applied magnetic field H_a and the domain wall width Δ.

This simple model also predicts how the domain wall velocity will depend on the thickness and width of the nanowire. From Eq (4.16) the velocity is dependent on the wall width Δ, which is a function of the transverse demagnetizing factor D

$$\Delta = \pi \sqrt{\frac{A}{K_{eff}}} \simeq \pi \sqrt{\frac{A}{2\pi D M_s^2}} \tag{4.17}$$

For an infinitely long wire, D is given as

$$D = 1 - \frac{1}{\pi}\left[\frac{1-p^2}{2p}\ln(1+p^2) + p\ln p + 2\arctan(\frac{1}{p})\right] \tag{4.18}$$

where $p = \frac{thickness}{width}$ [29]. For the nanowires used in these experiments, the thickness is 20 nm and the smallest width is $\sim$ 300 nm giving the largest p of 0.07. Therefore we can make the approximation that for $p \ll 1$, $D \sim p$ so then

$$\Delta = \pi\sqrt{\frac{A}{2\pi D M_s^2}} = constant \times \sqrt{\frac{width}{thickness}} \tag{4.19}$$

The derivation of Eq (4.16) can be used for high magnetic fields if the width of the domain wall is allowed to vary, although there is a transition point resulting from the upper limit of the demagnetizing torque. The torque from the applied magnetic field is simply proportional to the field and as such can increase indefinitely. The demagnetizing torque is proportional to $\sin 2\theta$ and has an upper limit when $\sin 2\theta = 1$. When the canting angle reaches $\theta = 90^\circ$ the sign of the demagnetizing torque changes and causes the domain wall to move in the opposite direction. This process repeats when the canting angle reaches $\theta = 180^\circ$ and the domain wall is once again in the plane of the sample, although in the opposite rotation direction. The overall velocity in this regime is still expected to be positive and non-zero, although much lower than the steady-state translational regime.

The transition from a steady-state domain wall moving in an applied magnetic field to the more turbulent motion predicted at higher fields has come to be known as Walker breakdown after the scientist who first predicted

its existence [31]. As the applied magnetic field is increased past the Walker breakdown point, the canting angle of $\vec{M}$ will precess continuously around the applied field. The use of cylindrical coordinates (x, θ) becomes useful here where x is along the nanowire and applied magnetic field and θ is in the direction of precession around the applied field.

At high fields the effective field $\vec{H}_{eff}$ can be replaced by the applied field $\vec{H}_a$ as the demagnetizing torque will average out to zero. The torque from the demagnetizing field is $-\gamma\vec{M} \times \vec{H}_{dem} = const \cdot \sin(2\theta)$. This averages to zero as $\langle \sin(2\theta) \rangle_\theta = 0$. During each precession of $\vec{M}$ the demagnetizing field will have equal magnitudes in opposite directions.

Starting again with Eq (4.2), we evaluate each term in cylindrical coordinates and replace $\vec{H}_{eff}$ with $\vec{H}_a$. $\frac{d\vec{M}}{dt}$ then becomes

$$\frac{d\vec{M}}{dt} = \left(\frac{d\vec{M}}{dt}\right)_\theta \hat{\theta} + \left(\frac{d\vec{M}}{dt}\right)_x \hat{x} \tag{4.20}$$

The longitudinal term (x) was derived previously as Eq (4.9), however we must replace the domain wall width Δ with the average wall width Δ_{avg} as the anisotropy energy of the wall will vary with the canting angle. This results in

$$\left(\frac{d\vec{M}}{dt}\right)_x = \frac{M}{\Delta_{avg}} v\hat{x} \tag{4.21}$$

The angular term is simply proportional to the angular velocity of the wall precession ω

$$\left(\frac{d\vec{M}}{dt}\right)_\theta = \omega M\hat{\theta} \tag{4.22}$$

Combining the longitudinal term and the angular term gives

$$\frac{d\vec{M}}{dt} = \frac{M}{\Delta_{avg}} v\hat{x} + \omega M\hat{\theta} \tag{4.23}$$

The damping term in Eq (4.2), when expressed in cylindrical coordinates, becomes

$$\alpha \frac{\vec{M} \times \frac{d\vec{M}}{dt}}{M} = \alpha \left[\left(\frac{d\vec{M}}{dt} \right)_{\theta} \hat{x} - \left(\frac{d\vec{M}}{dt} \right)_{x} \hat{\theta} \right] \tag{4.24}$$

After making all the substitutions, the final version of Eq (4.2) at high fields in cylindrical coordinates becomes

$$\frac{M}{\Delta_{avg}} v\hat{x} + \omega M\hat{\theta} = \gamma H_a M\hat{\theta} + \alpha M\omega\hat{x} - \alpha \frac{M}{\Delta_{avg}} v\hat{\theta} \tag{4.25}$$

Separating out the scalar components of Eq (4.25) results in

$$\hat{\theta} : \omega M = \gamma H_a M - \frac{\alpha M v}{\Delta_{avg}} \tag{4.26}$$

and

$$\hat{x} : \frac{Mv}{\Delta_{avg}} = \alpha M\omega \tag{4.27}$$

The scalar components can then be used to solve for ω and v,

$$\omega = \gamma H_a \tag{4.28}$$

$$v = \frac{\gamma \Delta_{avg}}{\alpha + \frac{1}{\alpha}} H_a \tag{4.29}$$

The velocity of the domain wall in the precessional regime has a similar form to the of the low magnetic field regime presented in Eq (4.16), however the mobility will be much smaller since α is less than 1.

4.2.2 Domain Wall Mobility Measurement

The velocity of a single domain wall was measured for magnetic fields up to 70 Oe. The domain wall travelled through a nanowire with a width of 600 nm and a length of 35 μm. The resulting velocity dependence is shown in Fig 4.4. At the lowest fields, there is a linear region with a slope of 25 m/s/Oe. Above the Walker breakdown point of 4 Oe for this nanowire, there is a region with a negative slope. At $\sim$30 Oe, a second linear region appears with a slope of 2.5 m/s/Oe.

Qualitatively, this form agrees with our one dimensional model presented in the previous section. The lower field linear region corresponds to the rigid wall derivation resulting in Eq (4.16). Above the breakdown field, the high field linear region corresponds to the precessional regime resulting in Eq (4.29). Calculating the breakdown field from Eq (4.15) by setting $\sin 2\theta = 1$ and using values appropriate to Permalloy nanowires, $M = 8000$ Oe and $\alpha = 0.02$, gives a value of $H_c = 80$ Oe. This value is more than an order of magnitude larger than the measured value of 4 Oe indicating that there are limitations to using the one dimensional model.

In the one dimensional model, the only domain wall structure that can exist is referred to as a transverse wall. In a one dimensional transverse wall, the magnetization rotates continuously from one direction to the other as previously shown in Fig 4.3. In a two dimensional model, transverse walls are still possible, as seen in Fig 4.5a, but a second configuration is available that is called the vortex domain wall. In a vortex domain wall, the magnetization

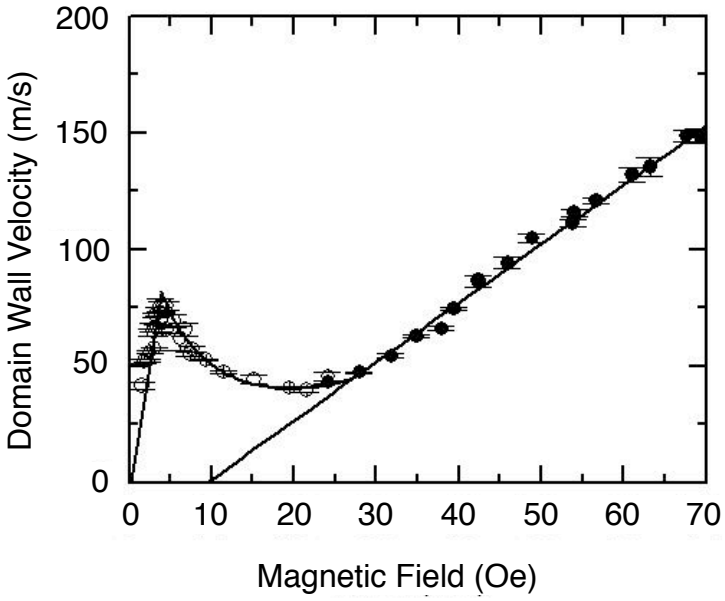

Figure 4.4: Domain wall mobility measurement using a nanowire with a width of 600 nm. The low field regime is linear up to the breakdown point of 4 Oe. A second linear regime occurs at higher fields.

rotates around a central spot called the vortex core. The magnetization for a vortex domain wall is shown in Fig 4.5b. Energy calculations have shown [32, 33] that a phase boundary exists between transverse and vortex domain walls of the form $w \cdot t \approx 60 L_{ex}^2$ where the exchange length $L_{ex} \approx 5$ nm for Permalloy. The phase boundary for domain walls in Permalloy nanowires is plotted in Fig 4.5c.

The high breakdown field predicted by the one dimensional model is lowered by the nucleation of a vortex [34]. The precession of the one dimensional model is then replaced by the movement of the vortex core across the width of the nanowire. The domain wall will move forward until the vortex core crosses the midpoint of the wire. The domain wall then moves backwards until the vortex core reaches the opposite edge of the nanowire. The energy required to nucleate a vortex is much lower than that required for large angle precession thus explaining the much lower breakdown field and transition to the oscillatory motion of the domain wall.

The numerical simulations conducted in [34] predict a breakdown field of $\sim$12 Oe which is much closer to our measured value of 4 Oe. This suggests that the rigid wall model used in the one dimensional derivation of the domain wall mobility is only valid at small canting angles. Above the breakdown field it is favorable to dissipate energy through vortex creation and propagation.

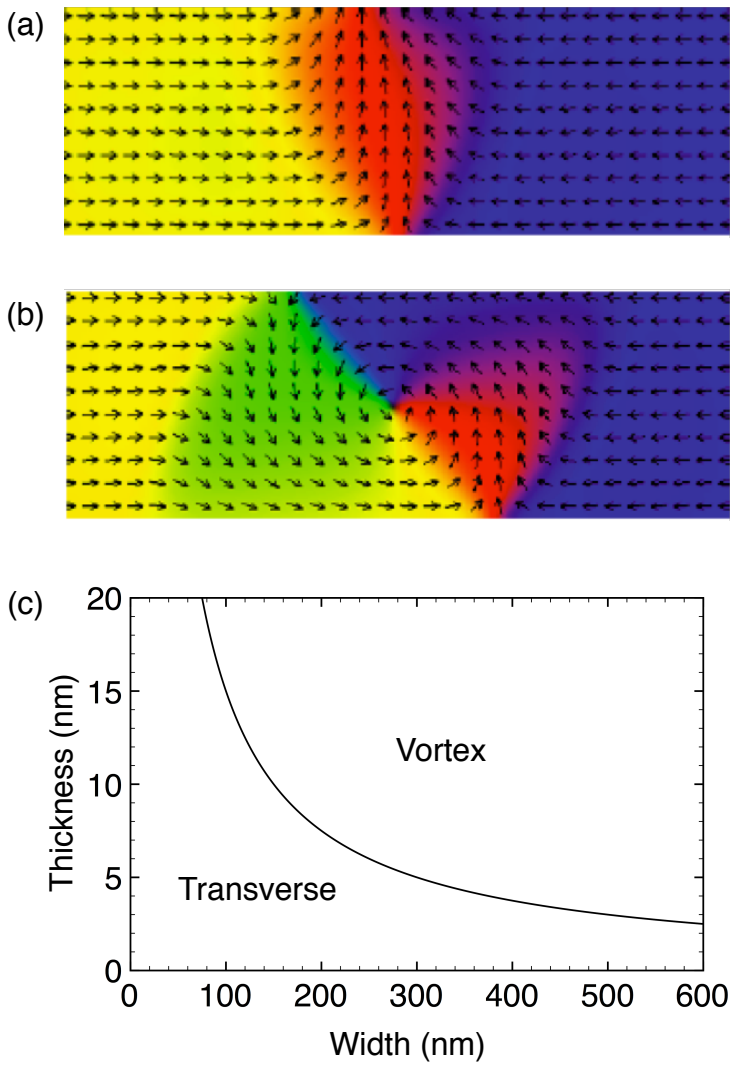

Figure 4.5: Approximate magnetization structure of transverse (a) and vortex (b) domain walls calculated using micromagnetic simulations. Energy calculations of these two types of walls result in a phase boundary (c) for domain walls in Permalloy nanowires.

4.3 Domain Wall Dynamics in Nanowires of Varying Width

As indicated in Eqs (4.16) and (4.29), the velocity of the domain wall depends not only on the applied field, but also on the domain wall width. According to Eq (4.19), the width of the domain wall is related to the width w of the nanowire with $\Delta \propto \sqrt{w}$. To observe this relationship between the domain wall velocity and nanowire width, the mobility curves for nanowires of a large range of widths were measured. The widths of the nanowires ranged from 310 nm to 2320 nm. The mobility curves of five of these wires are shown in Fig 4.6.

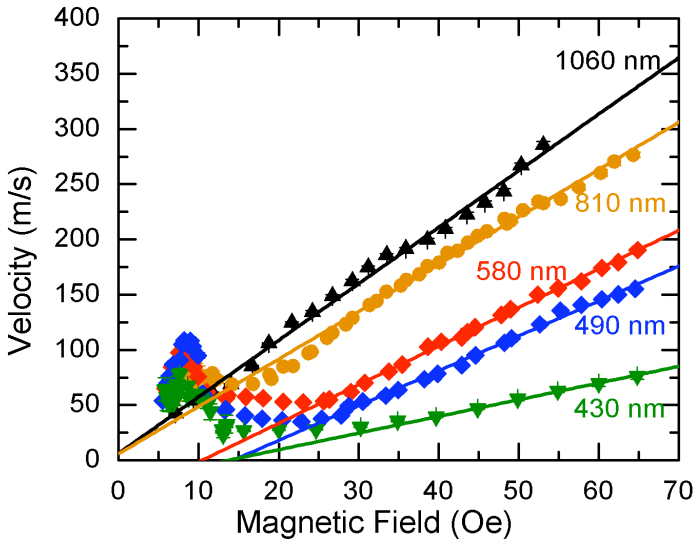

Figure 4.6: Mobility curves for nanowires of varying width. The high field mobility increases as the nanowire width increases.

The mobility of the high magnetic field region was measured for each nanowire. This region is defined by the linear section of the mobility curve that occurs above the Walker breakdown critical field. The high field mobility values are plotted in Fig 4.7 and are fit to a $\sqrt{w}$ function.

For nanowires of widths greater than ~900 nm, the Walker breakdown feature did not appear in the range of fields where the velocity was measured. The lowest fields measured were limited by the propagation field of each nanowire. While the low field mobility could be measured for a small number of nanowires, the variance and uncertainty in these values were too high to verify a relationship between nanowire width and low field mobility.

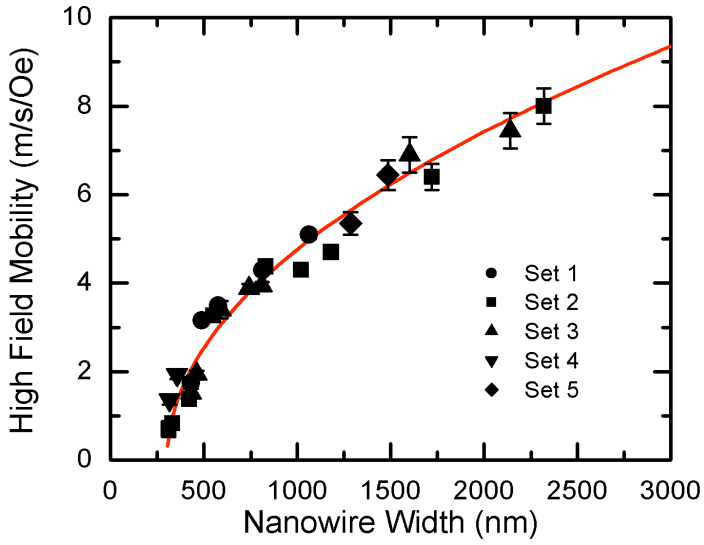

Figure 4.7: The high field domain wall mobility for various widths of nanowires. The red line is a fit to a $\sqrt{w}$ function. The fit intersects the x-axis at ~300 nm.

It is interesting to note that the functional relationship plotted in Fig 4.7 indicates that the domain wall high field mobility will reach zero at a non-zero nanowire width of about 300 nm. This seems to indicate that the width of the magnetic material in the nanowire is not the same as the physical width of the nanowire. Each wire then has approximately 150 nm of non-magnetic material along each edge. Since the initial continuous permalloy film is entirely magnetic, this nonmagnetic "dead" layer must originate from the FIB fabrication method.

While this mechanism has not been detailed in depth, one possibility is that the high energy ion beam causes the tantalum capping layers to mix with the permalloy along the edge of each structure. The phenomenon of the dead layer resulting from FIB patterning has been previously observed in experiments involving multilayer spin-valve sensors [35], CoFe films [36], and NiFe films [37]. In all three cases, Ta was used either as capping layers or for electrical contacts prior to FIB patterning. Studies of NiTa alloys have shown that as the percentage of Ta increases, the Ni transitions from ferromagnetic to paramagnetic to amorphous [38, 39].

4.4 Current Driven Domain Wall Dynamics

The interaction of spin-polarized current with domain walls was first described in 1978 by Luc Berger [40]. Since then, a number of additional theoretical works have expanded on the initial idea [41, 42, 43, 44, 45, 46]. Experiments have been conducted that attempt to infer the interaction of

current on domain wall dynamics [47, 48, 25, 49, 50]. The MOKE polarimeter setup used in this dissertation provides the ability to directly measure the change in velocity caused by the application of current [51].

4.4.1 Current Induced Torques on Domain Walls

In order to describe the dynamics of domain walls in the presence of current density j, additional terms must be included in the LLG equation. The full LLG equation then takes the form

$$\frac{d\vec{M}}{dt} = -\gamma\vec{M} \times \vec{H}_{eff} + \alpha\frac{\vec{M} \times \frac{d\vec{M}}{dt}}{M} - v_j\frac{d\vec{M}}{dx} - \beta v_j\vec{M} \times \frac{d\vec{M}}{dx} \tag{4.30}$$

Here the first two terms are the usual effective field torque and damping terms found in Eq (4.2). The third and fourth terms are current induced torques on the magnetization with $v_j = \eta j$. These two terms are referred to as the adiabatic and nonadiabatic torques, respectively. The strengths of these torques are determined by the parameters η and β.

The adiabatic term in Eq (4.30) has a widely accepted microscopic basis. A conduction electron passing through a domain wall will experience a torque from the changing magnetization. This torque will cause the spin of the electron to follow the magnetization of the domain wall. The change in angular momentum of the conduction electron is then transferred to the localized spins in the domain wall. The adiabatic parameter η is defined as

$$\eta = \frac{g\mu_B P}{2eM_s} \tag{4.31}$$

In this equation, g is the Landé factor, μ_B is the Bohr magneton, e is the electric charge, M_s is the saturation magnetization, and P is the spin polarization of the conduction electrons.

The source of the nonadiabatic torque is not quite as clear. Various competing theories have been put forth, but a consensus agreement has not yet been achieved. Experiments involving torques on domain walls resulting from current must then treat this term as a phenomenological parameter whose value is to be determined by the experimental results.

In the one dimensional model, the effects of the spin torque on the velocity of domain walls can be separated into terms for fields below Walker breakdown in the rigid wall regime and for fields far above breakdown in the precessional regime [52, 53]. Below breakdown, the velocity from Eq (4.16) is augmented by a term depending on the current and becomes

$$v = \mu H + \frac{\beta}{\alpha}\eta j \tag{4.32}$$

In the precessional regime the velocity from Eq (4.29) becomes

$$\langle v \rangle \rightarrow \alpha^2 \mu H + \eta j \tag{4.33}$$

Since only the adiabatic parameter is present in Eq (4.33) the precessional regime can be used to determine the influence of the adiabatic torque.

4.4.2 Current Driven Mobility Measurements

The nanowire configuration used in the previous sections in this chapter was designed to observe a single domain wall. This was achieved by discon-

necting one end of the nanowire from the continuous film. However, in order to have current flowing through the material both ends of the nanowire must be kept connected. In addition, a contact pad must be created in the continuous film such that the two ends of the nanowire are electrically isolated from each other aside from the path through the nanowire itself. Such structures were described in Section 3.1 and shown in Figs 3.3 and 3.4.

The contact pads were created with dimensions large enough to accommodate wire bonds from a wire bonding machine (West Bond 7476D-79). Current was then applied to the nanowire using a constant current source (Keithley 2400).

Domain wall velocity measurements were then carried out at various values of DC current. The resulting mobility curve is shown in Fig 4.8 with $j = 0$ for the black circles and $j = \pm 5.8 \times 10^{11} A/m^2$ for the blue and red circles. Both the low and high field mobilities are not changed significantly indicating that the current does not change the effective wall width.

The addition of current of both polarities results in a vertical shift in the domain wall mobility curve. From Eq (4.32) for fields below Walker breakdown, this shift indicates that the nonadiabatic spin torque term β, regardless of origin, has a non-zero value. Although it is not entirely clear how to extend this one dimensional model to vortex walls, any developments in theory must include this term.

The velocity of the domain wall is not shifted equally for opposite po-

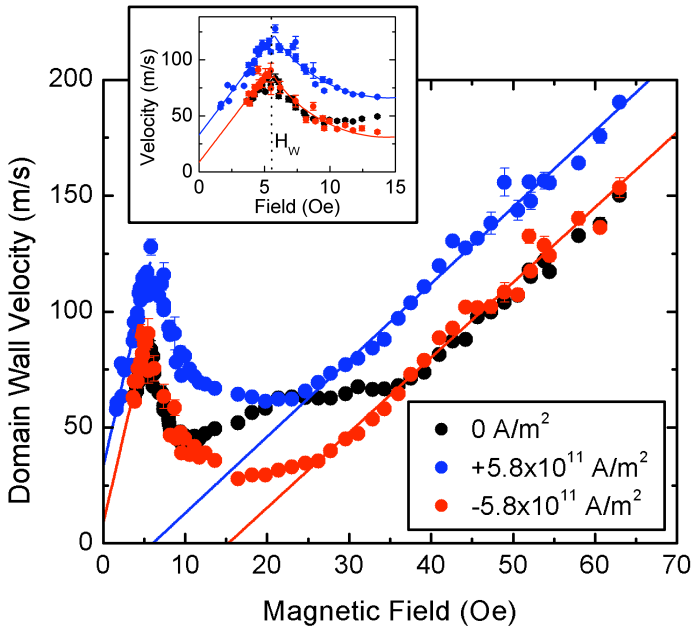

Figure 4.8: Domain wall mobility measurements under the influence of current. The zero current measurement is in black while the positive and negative current measurements are in blue and red, respectively.

larities of current and at some driving fields both polarities of current cause a positive shift. The effect of the current is therefore non-linear. This is evident in Fig 4.9a which shows how the domain wall velocity at a single driving field of 45 Oe changes with current.

Analysis of this measurement is made more clear by separating the complex current dependence into the even and odd components, v_+ and v_-, where $v_\pm = \frac{v(+j)\pm v(-j)}{2}$. The resulting odd component, shown in Fig 4.9b, is linear in j while the even component, shown in Fig 4.9c, has a quadratic form. The linear form of v_- corresponds to the adiabatic torque term of Eq (4.33).

The same measurement was carried out for nanowires with various widths. The velocity was measured as a function of current at a driving field of 45 Oe. When separated out into the odd and even components, shown in Fig 4.10a and b, the odd component shows a dependence on width. The adiabatic torque term in Eq (4.33) does not depend on width, so the current dependent velocity measurement in Fig 4.10a should remain constant with width. While a solid explanation for this width dependence is needed, possible causes could include edge roughness or the nonmagnetic dead layer discussed in Sec 4.3.

The even component does not depend on width but instead falls into two distinct quadratics. At this time it is not clear what determines the quadratic parameters of the even component. A simple width dependence is unlikely as increasing the width causes the even component to jump from one quadratic to the other and back. A broader survey of nanowires is required to provide further insight.

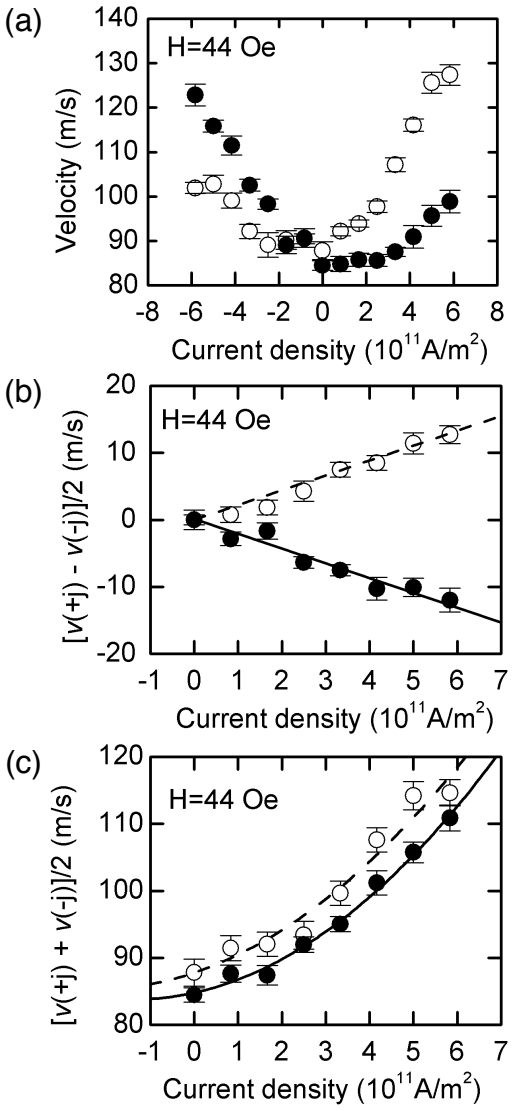

Figure 4.9: Domain wall velocity as a function of current density at a driving field of 44 Oe (a) separated out into odd (b) and even (c) components. The odd component has a linear form while the even component is quadratic.

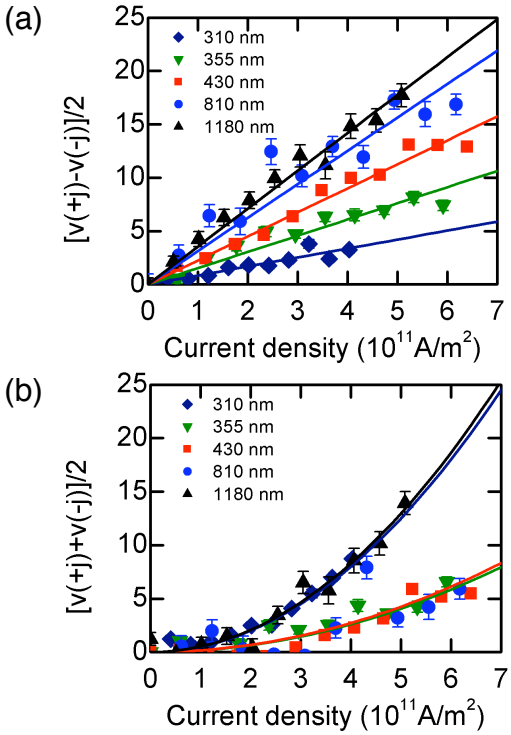

Figure 4.10: The odd (a) and even (b) components of velocity measurements for nanowires of various widths as a function of current. All measurements were conducted at a driving field of 45 Oe. The odd component is linear with the slope depending on width. The even component is quadratic and does not depend directly on width.

One unexpected feature that appeared in the initial measurement in Fig 4.8 is the "bump" that appears in the zero current mobility curve at ∼23 Oe. This bump was not seen in previous measurements and seems to have been suppressed with the addition of current in this nanowire. While the source of this bump was initially unknown, preliminary results of a more recent experiment have begun to shed light on this feature. The latest measurements involve applying a DC bias magnetic field perpendicular to the nanowire and the main driving field but still in the plane of the continuous film. This causes the bump in the mobility curve to grow with increasing perpendicular field causing the domain wall to traverse the nanowire at velocities higher than even those seen at the highest driving fields in other nanowires.

Preliminary micromagnetics simulations of a domain wall in this magnetic field arrangement show a second vortex core nucleating at the nanowire edge opposite the usual single vortex core. This dual-core domain wall configuration seems to reduce or even eliminate the turbulent domain wall oscillations that occur above the breakdown field. This returns the domain wall to a steady state motion through the nanowire allowing it to achieve much higher velocities. At the time of this writing, further experiments and simulations are in progress that should allow for a full understanding of this mechanism.

Chapter 5

Domain Wall Injection

In the previous chapter, the motion of domain walls in nanowires was discussed in depth. However, those domain walls entered each nanowire from the continuous film in a mechanism we call injection. This concept is one aspect of understanding how domain walls move across pinning sites in magnetic materials as well as in magnetic elements of varying shape or size. This chapter will discuss how domain walls enter a nanowire from the continuous film.

5.1 Injection via Thermal Activation

A domain wall moving through a magnetic material does not move in an absolutely smooth manner but instead moves in many small discontinuous steps. This process is known as the Barkhausen effect [1]. The Barkhausen effect is a result of surface/interface features, impurities, and lattice defects that act as small pinning sites for the movement of a domain wall [54].

The irreversible stochastic nature of the Barkhausen effect makes the study of any single pinning site impossible. This section will present the pinning of a domain wall at the interface between a nanowire and the continuous film as a model system for a single pinning potential. A pinned domain wall

is able to overcome the potential through thermal fluctuations in the domain wall when enough time is allowed to pass.

The observation of a domain wall becoming injected into the nanowire via thermal fluctuations begins with an area free of domain walls. To remove all domain walls, a strong magnetic field is first applied in one direction to saturate the magnetization of both the nanowire and the continuous film. A constant magnetic field of a magnitude below the field required to completely inject the domain wall is applied in the opposite direction. Since the continuous film has a lower anisotropy than the nanowire it will switch its magnetization at a very low field. The domain wall then becomes trapped by the pinning potential at the location where the nanowire is connected to the continuous film. This location is referred to as the neck of the nanowire. Thermal fluctuations in the domain wall give it a chance of overcoming the pinning potential resulting in the injection of the domain wall. The field is kept constant until the magnetization in the nanowire changes, indicating that the domain wall has entered and traversed the nanowire.

The waveform used for domain wall injection delay measurements consists of three pulses. The first pulse is in the positive direction and is used to determine if the domain wall has been injected. The waveform is set up in such a way that for each repetition of the waveform, this pulse analyzes the injection from the repetition immediately before it. This pulse is of the same polarity as the field being tested. If the domain wall has not been injected, this pulse has an amplitude large enough to inject the domain wall. If the domain

wall has been injected, then this pulse has no effect on the magnetization.

The other two pulses arrive 300 μs after the analyzing pulse. They are immediately adjacent to each other and of equal amplitude but opposite polarity. These two pulses act as initializing pulses to saturate the device in the positive direction and then in the negative direction. The section of the waveform after these two pulses produces no field by the high bandwidth magnet. However a Helmholtz coil magnet to the side of the sample produces a DC bias field at the level required for the measurement, a positive field much smaller than the initializing amplitude.

The time between the initialization pulses and the analyzing pulse is varied by adjusting the repetition rate of the arbitrary magnetic field waveform produced by the function generator. The repetition rate represents a period imposed on the waveform by the generator. The function generator used in the polarimeter setup can repeat an arbitrary waveform at rates from 0.001 Hz to 10 kHz, giving an upper limit of 1000 seconds to measure the injection delay.

Since each measurement consists of the averaged signal of at least 500 repetitions of the waveform, the resulting Kerr signal can be used to determine the probability that the domain wall was injected. A 500 μs measurement window is centered on the 300 μs section of the arbitrary waveform with the three pulses. The amplitude of the Kerr transient corresponding to the two initializing pulses is used as the reference amplitude. The amplitude of the Kerr transient resulting from the analyzing pulse is then the signal amplitude.

If the signal to reference ratio is 1, that corresponds to a 100% probability that the domain wall was *not* injected. If this ratio is zero, then the domain wall has a 0% chance of not being injected. The benefit in measuring both transients is that the ratio will remain valid even if the overall amplitude changes due to signal fluctuations.

For each field set by the DC bias coil the repetition rate is varied to increase the period of the waveform. The delay time associated with each measurement is then the period minus the 300 μs gap present in the waveform between the analyzing pulse and the initializing pulses. The probability that the domain wall is not injected into the nanowire is then plotted for each value of the delay time. A few examples of data from probability measurements are shown in Fig 5.1. This data is fit to an exponential of the form $e^{-t/\tau}$ where τ is then the time constant of injection delay for that field value.

The injection delay time was measured for four nanowires with widths varying from 490 nm to 1060 nm. For each nanowire the delay time was measured out to at least eight seconds. Since the injection time normally takes 10^{-8} seconds or less, this gives delay times spanning nine decades. The results from these measurements appear in Fig 5.2. For each wire, two field ranges become apparent. These two regions are more apparent when the injection delay measurements are shifted horizontally as in Fig 5.3.

The first region is at higher fields. In this field range, the slope of the injection delay time is the same for all nanowire widths. The motion of the domain wall in this region is determined by the LLG equation, Eq (2.11).

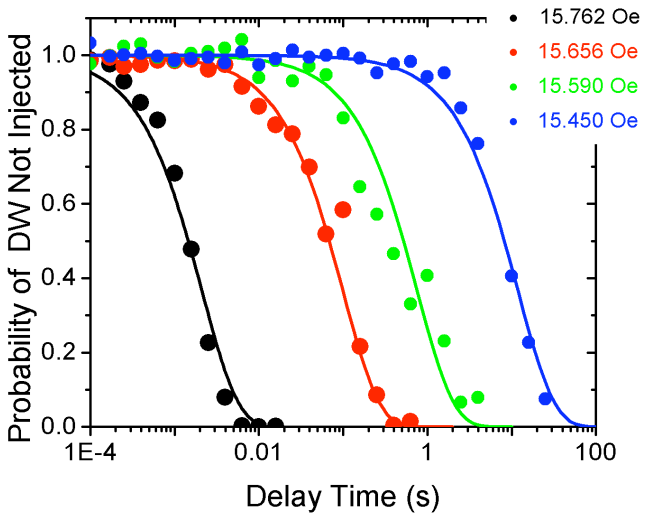

Figure 5.1: These measurements determine the injection delay time for a specific DC bias field. Each line represents a different field value. The period of the measurement waveform is varied and is used to determine the delay time for each point. The ratio of the signal Kerr amplitude to the reference Kerr amplitude then determines the probability that the domain wall is not injected.

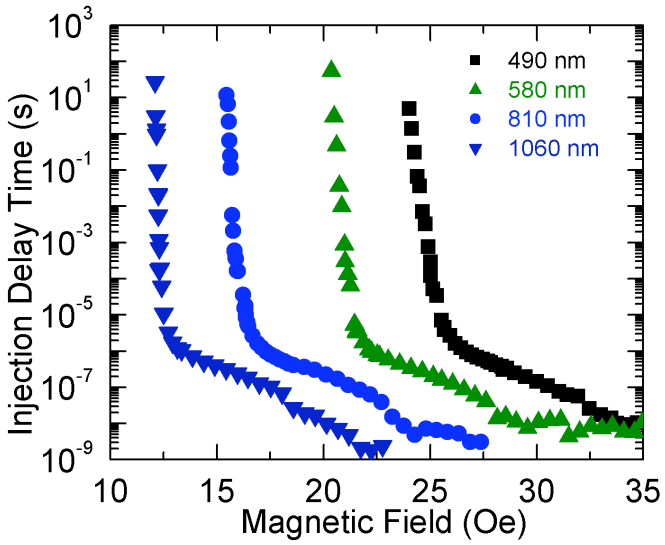

Figure 5.2: The injection delay measurement for four wires of various widths was measured with time delays spanning nine decades. In the high slope region domain wall thermal activation dominates the injection mechanism. In the low slope region spin rotation dominates.

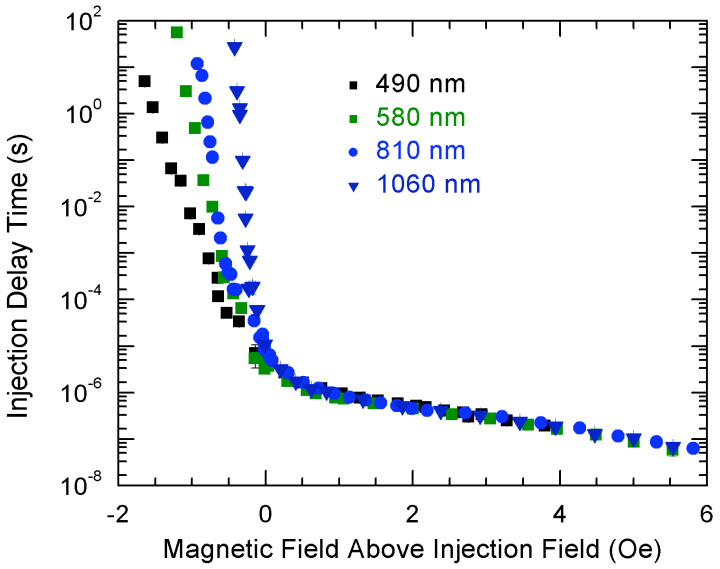

Figure 5.3: The injection delay measurements of Fig 5.2 are shifted horizontally such that the higher field region overlaps. The slope of the lower field region varies with nanowire width.

Using this equation the time delay τ_{spin} can be estimated to first order as

$$\tau_{spin}(H) \propto \frac{1}{\gamma(H - H_p)} \tag{5.1}$$

Here H_p is the intrinsic pinning field. Since this time delay does not depend on width it is the same for each nanowire.

As the field is decreased, a critical field is reached and the energy from the external field can no longer overcome the pinning potential at the neck of the nanowire. The pinning potential is related to the activation volume associated with the pinning site. The activation volume refers to the volume of spins that contribute to the energy of the pinning site. In the case of a nanowire, the difference in energy results from the magnetostatic energy from the stray fields in the domain wall at the edge of the nanowire that would not be present in a continuous film. In a nanowire of thickness t, the magnetostatic energy is greatest at the edge and decreases by one half at a distance of $t/2$ from the edge [32]. This area then extends the length of the domain wall Δ resulting in an approximate activation volume V of $V \sim t^2\Delta/2$.

Below the critical field the injection delay transitions to a region with a much higher slope that depends on the width of the nanowire. This critical field is the injection field. The injection delay can be modeled by a thermal activation model [55] that defines the injection delay time τ_{activ} as a function of applied magnetic field H

$$\tau_{activ}(H) = \tau_0 \exp\left(\frac{2M_sV}{k_BT}(H_p - H)\right) \tag{5.2}$$

Here τ_0 is an intrinsic pinning time, V is the activation volume, and k_BT is the thermal energy. Since the activation volume depends on the width of the nanowire the slope of this region increases with nanowire width.

The size of the pinning potential can be determined by the energy associated with the critical, or injection, field. As the magnitude of the external field is increased from zero, the height of the pinning potential is lowered until it disappears at the injection field. As seen in Fig 5.2, the value of the injection field depends on the width of the nanowire. This dependence is discussed in more detail in the following section.

5.2 Injection and Nanowire Width

To measure the injection field for a nanowire, a domain wall must first become pinned at the neck of the nanowire. A magnetic field is applied with a magnitude large enough to saturate both the nanowire and the continuous film in one direction. The field then returns to zero and a small field in the opposite direction is applied. The continuous film will switch at a lower field than the nanowire causing a domain wall to become pinned at the nanowire neck.

If the applied field is increased, it will overcome the pinning potential of the nanowire and the domain wall will enter, or become injected into, the nanowire. The field at which the domain wall breaks free from the neck, or is depinned, is referred to as the injection field. This process is illustrated in Fig 5.4. In general, the injection field is larger than the minimum field required

to propagate the domain wall through the nanowire.

To show how this injection field can depend on the width of the nanowire, a simple model of the forces involved when the domain wall is pinned can be used. The force on the domain wall resulting from the applied field, H, is pushing the domain wall into the wire while the pinning force is keeping the domain wall at the neck, as shown in Fig 5.5. The force from the magnetic field is proportional to the magnetization and the cross sectional area of the domain wall, i.e. $F_H \propto (M \cdot H)(w \cdot t)$ where t is the film thickness and w is the width of the nanowire and hence of the cross section of the domain wall. F_p is the pinning force from the corners formed by the nanowire and the continuous film. The domain wall is injected when the force from the magnetic field overcomes the pinning force. This gives a critical magnetic field, H_{inj}, that is proportional to $1/w$

$$H_{inj} \propto \frac{2F_p}{Mt}\frac{1}{w} \tag{5.3}$$

In order to measure the injection field of a nanowire, a hysteresis loop measurement is performed on the wire. A strong magnetic field is applied in one direction to saturate the nanowire and the film. The field is then swept towards a magnetic field of equal magnitude but opposite direction. The magnetic field is then returned to the original value and direction at a continuous rate. Throughout all of these field changes, the magnetization is monitored using Kerr measurements at a fixed point on the nanowire. Examples of these hysteresis loops for nanowires of various widths are shown in Fig 5.6.

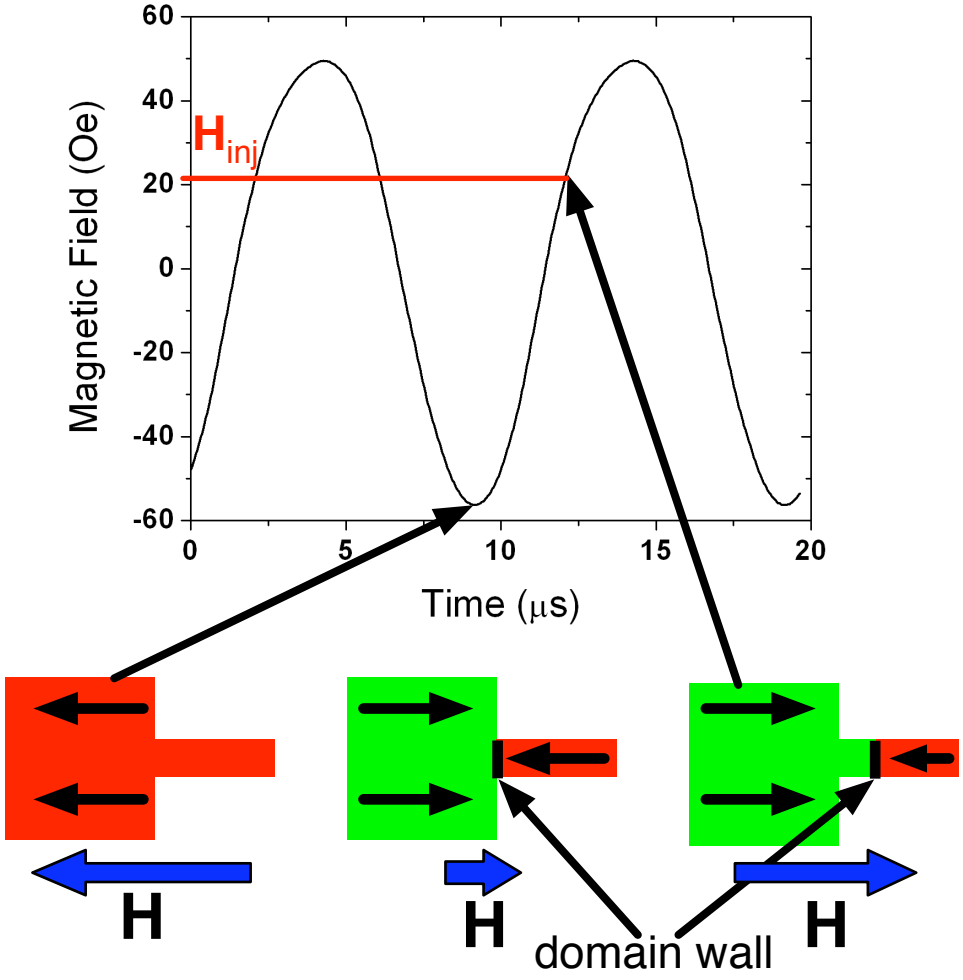

Figure 5.4: A large magnetic field first saturates both the nanowire and the continuous film. As the field is swept to the opposite polarity the continuous film switches first causing a domain wall to become pinned. When the field reaches the injection field the domain wall is injected into the nanowire.

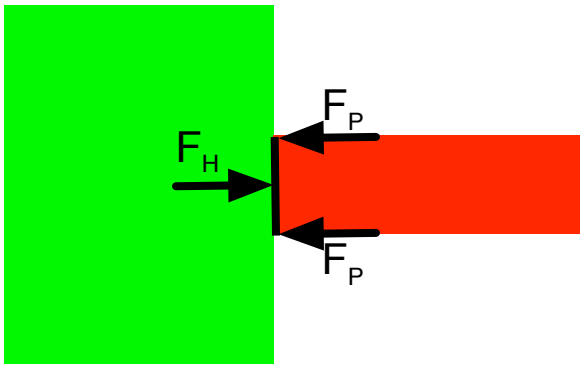

Figure 5.5: The force from the pinning potential at the neck of the nanowire acts against the driving force from the external magnetic field.

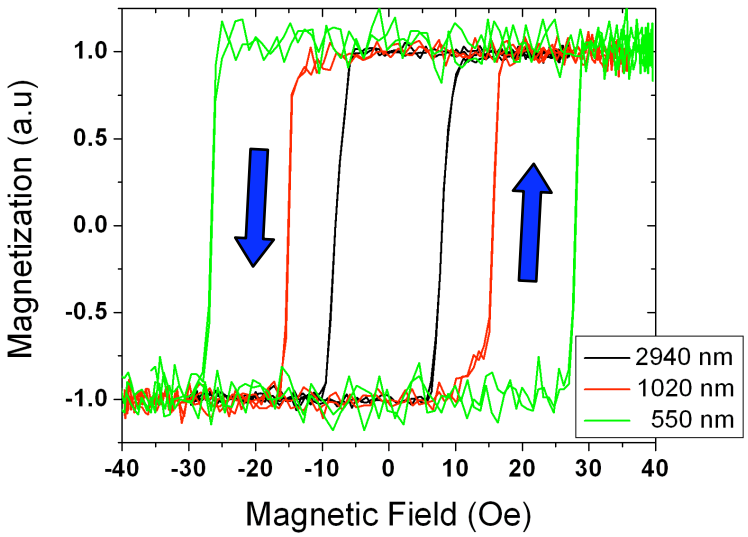

Figure 5.6: The magnetization of the nanowire is monitored using Kerr measurements as the magnetic field is varied. These three resulting hysteresis loops were measured on three nanowires with different widths. The field at which the magnetization switches is the injection field.

A 10 kHz sine wave was chosen to drive the magnet system during the hysteresis measurements. This frequency is fast enough so that averaging 10,000 loops or more to increase the signal to noise ratio will not require a large amount of time, but slow enough that the magnetic field does not change too quickly while the domain wall is traversing the nanowire. The waveform has a large enough amplitude to saturate the nanowire in both directions. MOKE measurements are then performed at a single point 10 μm from the neck of the nanowire. When the magnetic field waveform reaches the injection field, the nanowire switching will be recorded by the MOKE measurement. The MOKE signal is then matched with the magnetic field profile to create a hysteresis loop of the nanowire.

The injection field was measured for seven different nanowires with widths varying from 550 nm to 2940 nm. The results are shown in Fig 5.7. The red line on the plot is a fit of the data to a $1/w$ relationship. This aligns with the injection field defined in Eq (5.3) resulting from the model of the forces acting on the pinned domain wall.

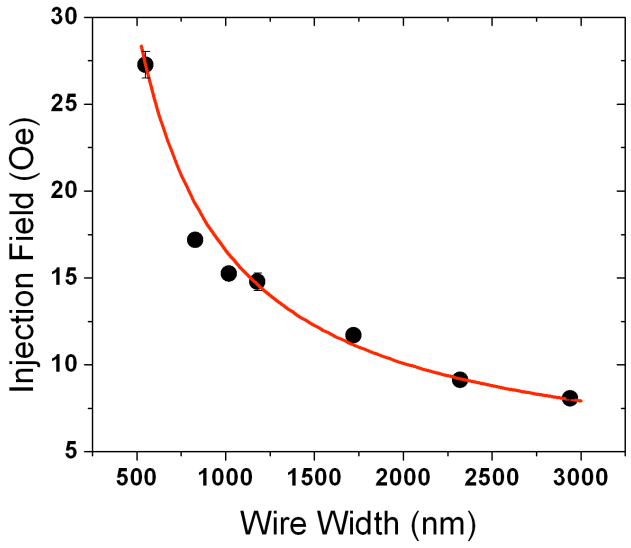

Figure 5.7: The injection field shows an inverse relationship to the nanowire width.

Chapter 6

Domain Wall Induced Voltage

In 1986, Luc Berger envisioned measuring the voltage across a moving domain wall at the same time that a current was passing through the material [56]. He calculated that the presence of the domain wall in motion would increase the usual ohmic voltage by an amount

$$V = -\frac{\hbar}{e}\frac{d\phi}{dt} + \frac{2M_s R_0}{\mu}(\beta v_e - v_w) \tag{6.1}$$

where $\frac{d\phi}{dt}$ is the precession of the domain wall magnetic moment, v_w is the velocity of the domain wall, v_e is electron drift velocity resulting from the current ($v_e = R_0 j_x$), R_0 is the ordinary Hall constant, μ is the domain wall mobility, and β is a dimensionless coefficient. It was estimated that this additional voltage would be on the order of nV. This voltage would be difficult to detect as the normal ohmic voltage would be many orders of magnitude larger. However, if there was no current so that $v_e = 0$, a domain wall driven by a magnetic field could produce a measurable signal. The fabrication and measurement techniques presented in previous chapters of this dissertation provide the methods required to conduct electrical measurements involving individual domain walls.

6.1 Measurement Methods

The voltage produced by a domain wall depends on the wall velocity, including both its magnitude and sign. If two domain walls were present in a nanowire moving with equal velocities but in opposite directions, the voltages produced would average to zero. In order to ensure that a single domain wall was present, one end of the nanowire must be cut. However, to make electrical measurements, the nanowire must have electrical contacts at both ends. This is achieved by placing platinum across the cut end of the nanowire using the GIS in the FIB, as described in Sec 3.1. A SEM image of the resulting wire with a detail of the Pt bridge can be seen in Fig 6.1.

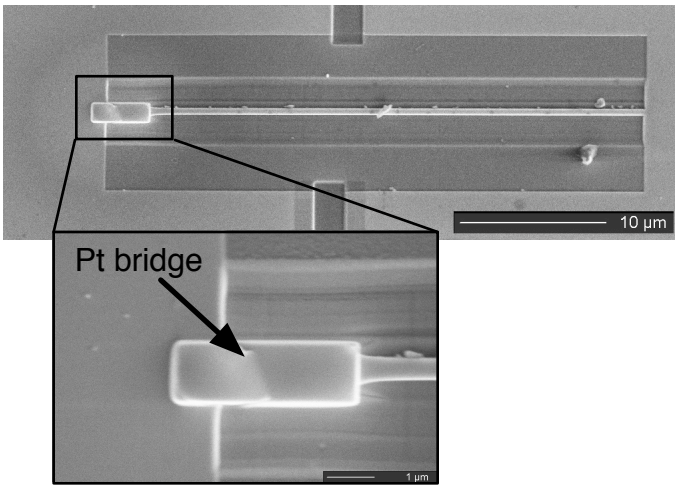

Figure 6.1: A nanowire used to study a single domain wall requires the the nanowire be cut at one end to ensure that only a single domain wall traverses the nanowire. This nanowire is modified for electrical measurements with the addition of a Pt bridge using the GIS in the FIB.

In order to maintain a voltage signal from the domain wall in motion,

the driving magnetic field must be chosen in such a manner to maximize the time during which a domain wall is traveling through the nanowire. A 300 kHz driving magnetic field provides the right amount of time for this nanowire in that it is long enough that the domain wall will traverse the entire nanowire but short enough that there is a minimal amount of time where the domain wall is absent. The amplitude of this driving field is sufficient to inject domain walls at both polarities.

The high frequency magnetic field induces a large voltage in the measurement wires at the driving frequency, so a modulation lock-in technique was used to measure the domain wall voltage. A small coil magnet was situated such that it produced a modulating magnetic field at the nanowire with an amplitude of 10 Oe at 317 Hz. A lock-in amplifier (Stanford Research SR510) was used to detect the signal at the modulation frequency. The details of this technique and the expected form of the resulting voltage measurement are explained in the following paragraphs.

The combination of the 300 kHz magnetic field and the 317 Hz magnetic field result in the three field profiles shown in Figure 6.2. Figure 6.2a is the 300 kHz magnetic field without any modulation. The dotted red lines indicate the injection field for the nanowire being used for the measurement. The unmodulated field is high enough to inject a domain wall at both polarities. Figures 6.2b and c show the field profile of the combined fields during the positive and negative segments of the modulation field. This results in the injection of a domain wall at only the first cycle of the 300 kHz driving field.

As the field in the opposite polarity in both cases is below the injection field, a domain wall will not be injected for any subsequent field cycles.

The measurement uses a third magnet to create a DC bias magnetic field that adds to the high frequency driving field and the low frequency modulation field. This magnet is then used to measure the lock-in voltage as a function of the DC bias field. The expected qualitative form of this measurement is presented in Fig 6.3. There are four segments of this measurement. During segment A, the bias field is large enough in the negative direction that no domain walls are injected. This results in no domain wall motion in the nanowire and zero domain wall voltage. At segment B, the bias field range allows domain walls to be injected only during the positive half of the modulation field. Since the lock-in amplifier is set up to measure on the falling edge, the voltage signal will be out of phase with the modulating field and results in a negative lock-in voltage. Once the bias field crosses zero, domain walls will be injected on the negative half of the modulation field only. This causes the domain wall voltage signal to be in phase with the modulation field resulting in a positive lock-in voltage, as shown in segment C. In segment D, the bias voltage again reaches an amplitude where no domain walls are injected and the domain wall voltage returns to zero.

6.2 Results and Discussion

The lock-in voltage measured using the technique described in the previous section resulted in the data shown in Fig 6.4a. The form of this measure-

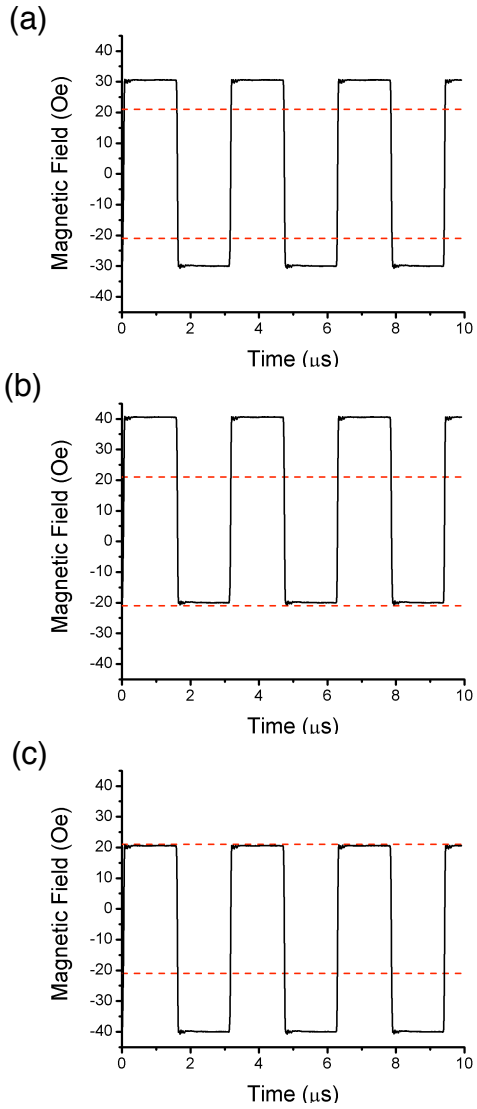

Figure 6.2: The 300 kHz magnetic field waveform used to drive the domain wall for domain wall voltage measurements (a) is modulated by a 300 Hz, 10 Oe magnetic field. The driving field is shifted up during the positive polarity of the modulation field (b) and down for the negative polarity (c).

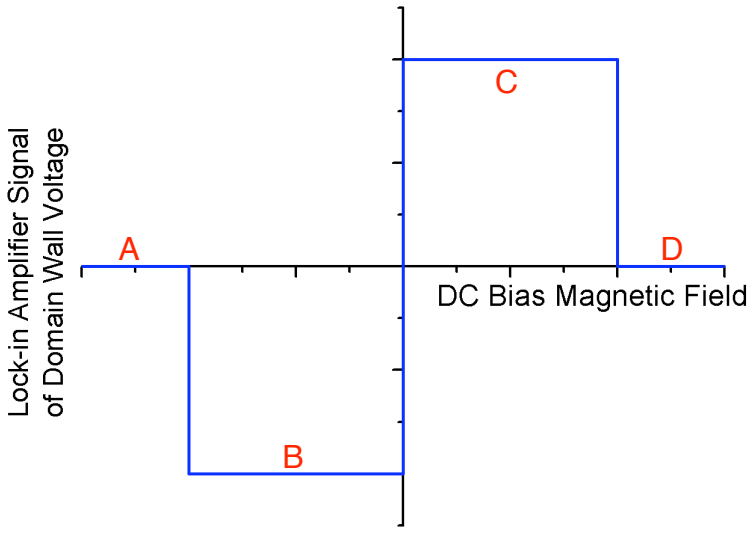

Figure 6.3: The expected form of the domain wall voltage measurement using a modulation technique. At points A and D the DC bias field is too large for domain walls to be continuously injected. When domain walls are continuously injected, the resulting voltage measured by the lock-in amplifier will be negative when the signal is out of phase with the modulation field (B) and positive when it is in phase with the modulation field (C).

ment is more complex than the expected form presented in Fig 6.3. However, it can be separated out into two components, even and odd. The even component V_+ and odd component V_- are calculated by $V_\pm = \frac{V(H_+) \pm V(H_-)}{2}$. The odd component, shown in Fig 6.4b, has the expected form of voltage induced by a moving domain wall and produces a domain wall voltage of ∼450 nV. The source of the even component, shown in Fig 6.4c, is unclear. Additional measurements were made to determine that the odd component was indeed a result of a moving domain wall.

The first test measured the odd component of the lock-in voltage as the period of the high frequency magnetic field waveform was decreased. The domain wall will only induce a voltage when it is moving and only during the time it takes for the domain wall to traverse the entire nanowire. This transit time is fixed by keeping the driving field, and thus the velocity, constant. Fig 6.5 shows four of the waveforms used in this measurement with varying periods.

Since the lock-in amplifier was measuring at the fixed frequency of the modulation field, the voltage measured is an average of any voltage signals over the period of the modulation field. Decreasing the period of the high frequency driving field increases the number of times the domain wall traverses the nanowire, each time adding to the average voltage measured by the lock-in amplifier. The result, as seen in Fig 6.6, is that the lock-in voltage increases until the period matches the domain wall transit time. Below the domain wall transit time, the driving field period is not long enough for the domain

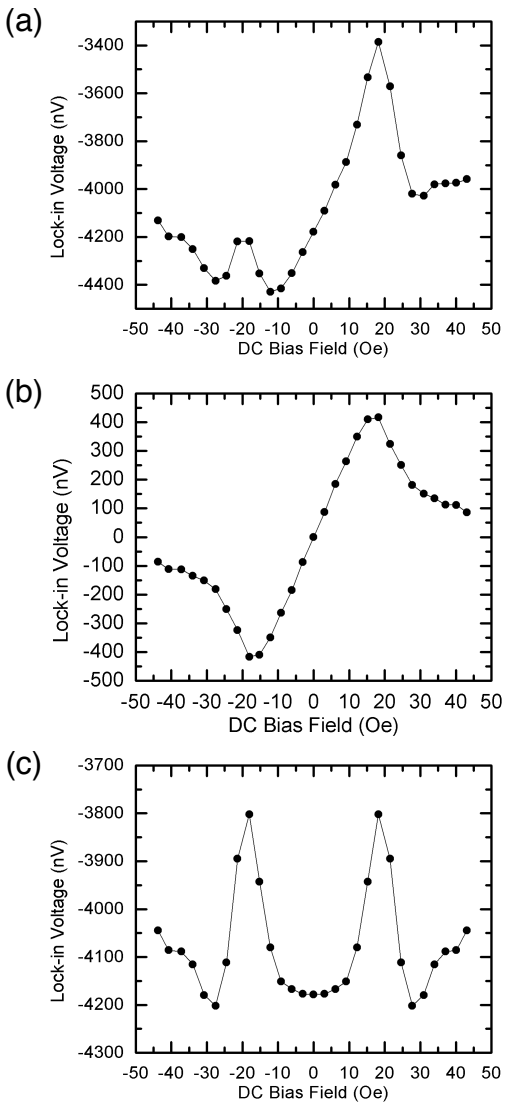

Figure 6.4: The voltage induced by a moving domain wall measured with a modulation technique (a), is then separated into odd (b) and even (c) components for analysis.

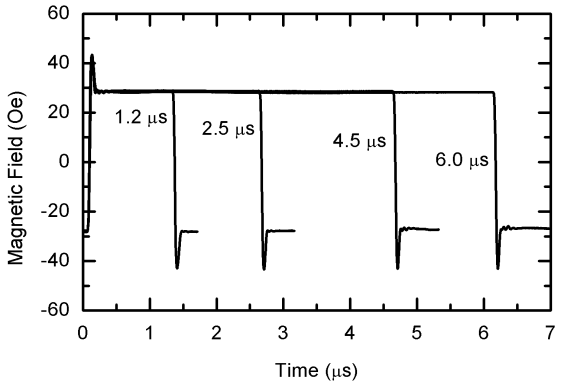

Figure 6.5: A series of magnetic field waveforms with decreasing period is used to correlate the transit time of the domain wall with the measured voltage.

wall to reach the end of the nanowire. When the polarity of the driving field changes, the domain wall will move in the opposite direction. At the same time, a second domain wall will enter the nanowire and move towards the first domain wall. The effect of having multiple domain walls moving in opposing directions causes the overall voltage to decrease.

A complimentary method of determining that the voltage measured does indeed originate from the moving domain wall is to measure the voltage at two magnetic field waveforms, one that will drive a domain wall and one that will not. A waveform with an amplitude below the injection field will not inject a domain wall and there will never be a domain wall present in the nanowire. To reduce any possible changes from using a drastically different waveform to drive a domain wall, the same waveform is used but it is altered slightly by adding an injection pulse at the beginning of each half-cycle. These two

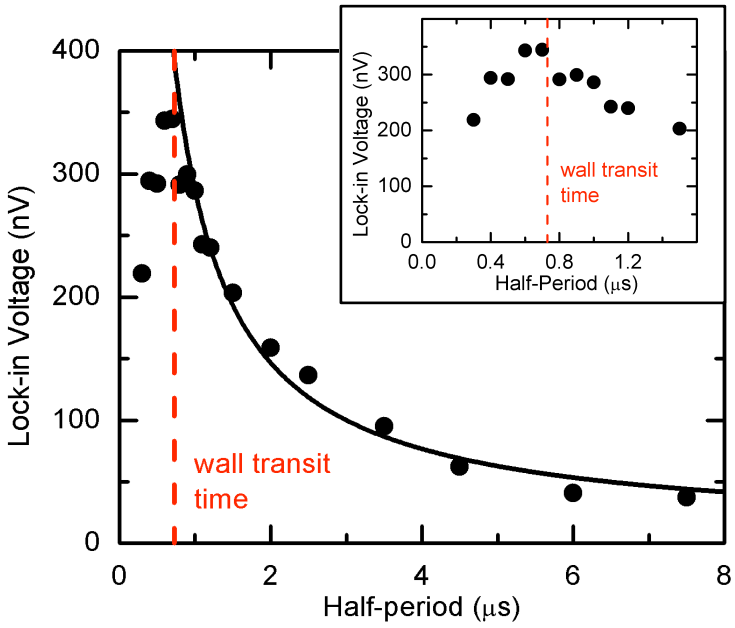

Figure 6.6: The domain wall voltage measured as the period of the driving magnetic field is decreased. The voltage reaches a peak at the wall transit time. Below the transit time the domain wall does not traverse the nanowire entirely causing a drop in the voltage measured, possibly due to multiple domain walls in the nanowire simultaneously moving in opposing directions.

waveforms are shown in Fig 6.7 with the black waveform below the injection field, indicated in red, and the blue waveform containing the injection pulse. This injection pulse overcomes the pinning potential at the neck of the domain wall and places the domain wall just inside the nanowire. The field then returns to the driving level as before and the nanowire traverses the wire. The presence or absence of a domain wall for these two waveforms was verified using MOKE measurements prior to the voltage measurements.

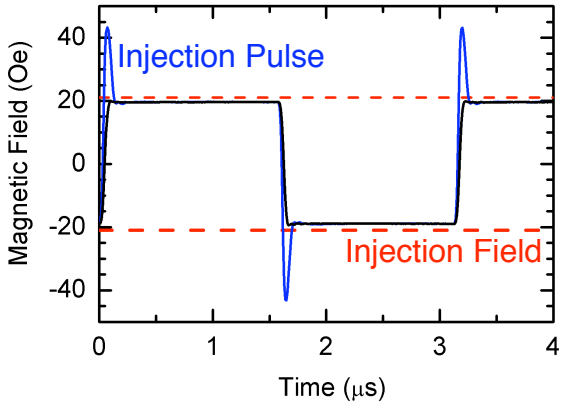

Figure 6.7: A driving magnetic field with and without injection pulses. The dashed red line indicates the injection field level. The magnetic field without the injection pulse is below the injection field. No domain walls will be injected into the nanowire when this waveform is used. The addition of the injection pulse allows the domain wall to enter the nanowire.

The voltage from the nanowire was then measured for both magnetic field waveforms. The raw data is shown in Fig 6.8a. The waveform without injection pulses resulted in the data shown in black while the waveform with the added injection pulses produced the data in red. This data again shows the complex structure seen before. When the data is separated out into the odd

and even components, a much clearer picture can be seen. The odd components, shown in Fig 6.8b, indicates that the measurement with the domain wall present produces a similar voltage profile as before. The voltage at this field is $\sim$150 nV. However, when a domain wall is absent from the measurement, the odd component produces a zero voltage reading within uncertainty. This is a clear indication that the voltage in the odd component of these measurements is indeed induced by the moving domain wall.

The existence of a non-zero even component of the voltage measurement, shown in Fig 6.8c, in the absence of a moving domain wall indicates that this component is not a result of the moving domain wall. The difference in this signal between waveforms with and without the injection pulse seems to indicate that the source of the voltage is related to the high frequency magnetic field. This should not be the case as the lock-in amplifier is locked to the much lower frequency of the modulation field and should not measure signals at the driving frequency. Further investigation is required to determine the exact source of this component of the voltage.

Having established the source of the odd component of the voltage as the moving domain wall, the amplitude of the voltage was measured at various amplitudes of the driving magnetic field. The results of these measurements are broken down into the odd component in Fig 6.9a and the even component in Fig 6.9b. The scaled domain wall voltage increases linearly with the domain

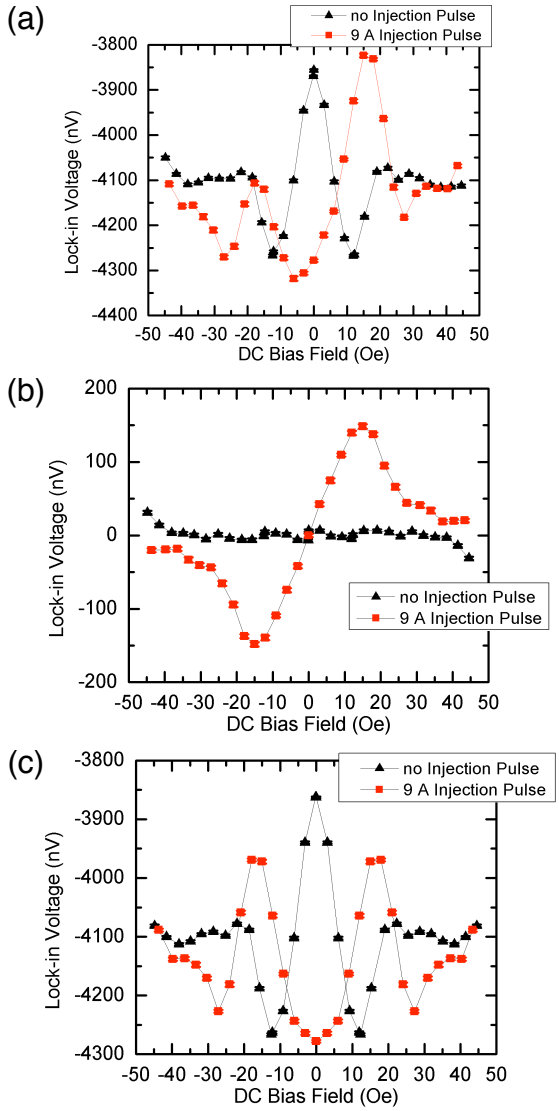

Figure 6.8: Voltage measurements in the absence of a domain wall (black) and with a moving domain wall (red). The raw data (a) is separated into the odd (b) and even (c) components. The odd component (b) shows no voltage when a domain wall is not present in the nanowire (black).

wall driving field, as shown in Fig 6.9c. The scaled voltage V_s is defined as

$$V_s(H) = V\frac{T}{2}\frac{L}{v_w(H)} \tag{6.2}$$

Here V is the raw voltage, T is the period of the driving magnetic field, L is the length of the nanowire, and v_w is the velocity of the domain wall at the driving magnetic field amplitude H. This scaling is necessary since the voltage signal is only produced when the domain wall is moving and the lock-in amplifier averages the voltage signal over the same time scale independent of the driving magnetic field.

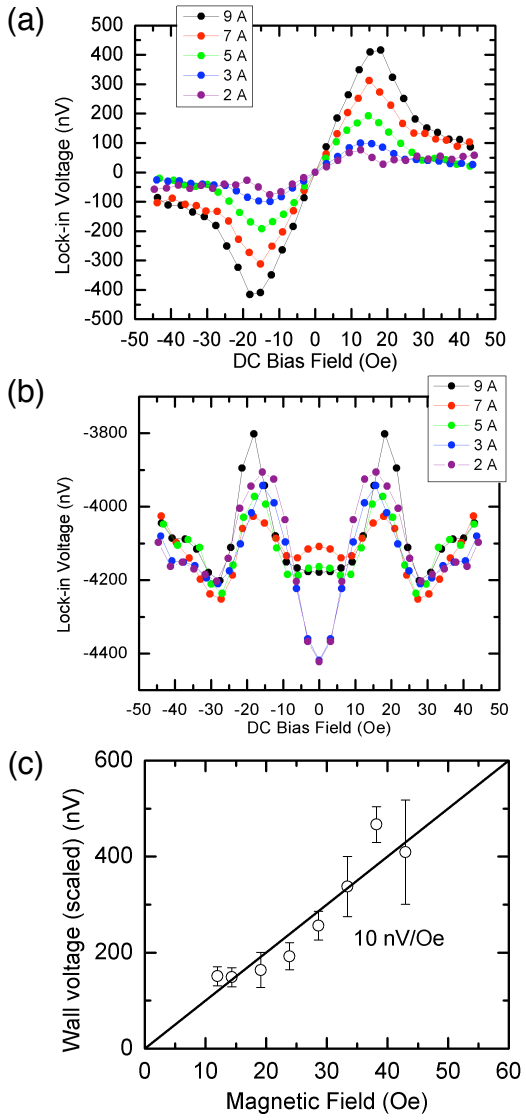

Figure 6.9: The odd (a) and even (b) components of voltage measurements of a moving domain wall at various driving fields. The scaled voltage increases linearly with driving field (c). The voltage is scaled to compensate for the averaging of the lock-in amplifier.

Chapter 7

Conclusions

The dynamics of magnetic domain walls in Permalloy nanowires fabricated using FIB patterning have been studied using a magneto-optical Kerr effect polarimeter. Two regimes emerge from these measurements. At fields below a critical magnetic field the motion of the domain wall is in a steady state. The domain wall translates smoothly with a linear domain wall mobility. Above the critical field, this steady state experiences a "breakdown" into a turbulent regime characterized by an oscillatory motion of the domain wall. At fields well above the critical field the mobility of the domain wall is again linear, but much lower than the steady state mobility.

The effects of the width of the nanowire on the domain wall mobility in the high field regime were observed. The domain wall mobility increases with the square root of the nanowire width. However, the domain wall mobility is zero at a non-zero nanowire width. This is presumed to occur due to nonmagnetic edges on each nanowire resulting from the FIB fabrication process. The measurements indicate a nonmagnetic "dead layer" of $\sim$150 nm on each edge of the nanowires.

The dynamics of domain walls under the influence of DC current were

observed. The current was found to increase the velocity of the domain wall at both polarities, although not symmetrically. Changes in velocity below Walker breakdown due to spin torque indicate a non-zero nonadiabatic spin torque parameter β. Further analysis of the velocity as a function of current revealed two separate terms in current, one linear and one quadratic. The linear term was found to increase with nanowire width while the quadratic term has no direct dependence on nanowire width.

A pinning potential at the neck of the nanowire will pin a domain wall at low fields. Thermal fluctuations in the domain wall structure allowed the domain wall to overcome the pinning potential causing the domain wall to become injected into the nanowire. The time required for the thermally activated injection is decreased with increasing field. Activation times were measured up to 10 seconds for four nanowires of varying width. The activation time decreases linearly with magnetic field on a logarithmic scale over 7 decades before reaching the critical injection field and transitioning to a second linear region with a lower slope. The slope of the initial region depends on the width of the nanowire as injection this region is described by a thermal activation mechanism which depends on the activation volume of the domain wall. The activation volume depends on the width of the nanowire. The low slope region has the same slope independent of nanowire width as the spin rotation mechanism involved in this region does not depend on the nanowire width.

The injection of a domain wall from a continuous film into a nanowire was studied for nanowires of various widths. The domain wall becomes pinned

at the neck of the nanowire due to the pinning potential. The minimum field required for the domain wall to become depinned from the nanowire neck, referred to as the injection field, was found to be inversely proportional to the width of the nanowire.

A moving domain wall was found to induce a voltage across the nanowire through which the domain wall is moving. The complex voltage produced by the measurement was found to be separable into even and odd components. The odd component was shown to correspond to the contribution of the voltage resulting from the moving domain wall. The origin of the even component is currently unknown. The voltage produced by the moving domain wall is on the order of hundreds of nV and is proportional to the velocity of the domain wall.

7.0.1 Recommendations for Future Work

Further work is required to fully explain the origin of the nonmagnetic "dead layer" induced by FIB patterning, particularly the lateral extent of the magnetic suppression. The hypothesis that the dead layer is induced by the mixing of Ta with the magnetic permalloy layer can be tested by using other suitable materials for capping layers.

All the measurements of domain wall injection via thermal activation were conducted at room temperature. A measurement of the temperature dependence of this mechanism would provide further information about the nature of the pinning potential.

Certain aspects of the measurements presented do not correspond to any theoretical model. These include the even component of the domain wall velocity as a function of current, the width dependence of the odd component of the domain wall velocity as a function of current, and the even component of the voltage induced by a moving domain wall. Either adjustments to the theory must be made or conclusive evidence that these are experimental artifacts must be presented to resolve these discrepancies.

Bibliography

[1] Soshin Chikazumi. *Physics of Ferromagnetism*. Oxford University Press, Oxford, 1997.

[2] Michael P. Marder. *Condensed Matter Physics*. John Wiley & Sons, New York, 2000.

[3] Joachim Stöhr and Hans Christoph Siegmann. *Magnetism: From Fundamentals to Nanoscale Dynamics*. Springer, Berlin, 2006.

[4] H. A. M. van den Berg. Self-consistent domain theory in soft-ferromagnetic media II. Basic domain structures in thin film objects. *Journal of Applied Physics*, 60:1104, 1986.

[5] L.D. Landau and E.M. Lifshitz. On the theory of the dispersion of magnetic permeability in ferromagnetic bodies. In D. ter Haar, editor, *Collected Papers of Lev Landau*, page 101. Gordon and Breach, New York, 1967.

[6] T.L. Gilbert. A phenomenological theory of damping in ferromagnetic materials. *IEEE Transactions on Magnetics*, 40(6):3443, 2004.

[7] Petros N. Argyres. Theory of the Faraday and Kerr effects in ferromagnetics. *Physical Review*, 97(2):334, 1955.

[8] Marvin J. Freiser. A survey of magnetooptic effects. *IEEE Transactions on Magnetics*, Mag-4(2):152, 1968.

[9] A. V. Sokolov. *Optical Properties of Metals*. American Elsevier Publishing Co., New York, 1967.

[10] C. Nistor, G. S. D. Beach, and J. L. Erskine. Versatile magneto-optic Kerr effect polarimeter for studies of domain-wall dynamics in magnetic nanostructures. *Review of Scientific Instruments*, 77(10):103901, 2006.

[11] M.N. Baibich, J.M. Broto, A. Fert, F. Nguyen Van Dau, F. Petroff, P. Eitenne, G. Creuzet, A. Friederich, and J. Chazelas. Giant magnetoresistance of (001)Fe/(001)Cr magnetic superlattices. *Physical Review Letters*, 61(21):2472, 1988.

[12] G. Binasch, P. Grünberg, F. Saurenbach, and W. Zinn. Enhanced magnetoresistance in layered magnetic structures with antiferromagnetic interlayer exchange. *Physical Review B*, 39(7):4828, 1989.

[13] S.A. Wolf, D.D. Awschalom, R.A. Buhrman, J.M. Daughton, S. von Molnár, M.L. Roukes, A.Y. Chtchelkanova, and D.M. Treger. Spintronics: A spin-based electronics vision for the future. *Science*, 294:1488, 2001.

[14] B. Dieny, V.S. Speriosu, S. S. P. Parkin, B.A. Gurney, D.R. Wilhoit, and D. Mauri. Giant magnetoresistance in soft ferromagnetic multilayers. *Physical Review B*, 43(1):1297, 1991.

[15] S. S. P. Parkin. Dramatic enhancement of interlayer exchange coupling and giant magnetoresistance in $Ni_{81}Fe_{19}$/Cu multilayers by addition of thin Co interface layers. *Applied Physics Letters*, 61(11):1358, 1992.

[16] D.M. Heim, R. E. Fontana, C. Tsang, V.S. Speriosu, B.A. Gurney, and M.L. Williams. Design and operation of spin valve sensors. *IEEE Transactions on Magnetics*, 30(2):316, 1994.

[17] S. Yuasa, A. Fukushima, T. Nagahama, K. Ando, and Y. Suzuki. High tunnel magnetoresistance at room temperature in fully epitaxial Fe/MnO/Fe tunnel junctions due to coherent spin-polarized tunneling. *Japanese Journal of Applied Physics*, 43(4B):L588, 2004.

[18] S. Yuasa, T. Nagahama, A. Fukushima, Y. Suzuki, and K. Ando. Giant room-temperature magnetoresistance in single-crystal Fe/MgO/Fe magnetic tunnel junctions. *Nature Materials*, 3:868, 2004.

[19] S. S. P. Parkin, C. Kaiser, A. Panchula, P.M. Rice, B. Hughes, M. Samant, and S.-H. Yang. Giant tunnelling magnetoresistance at room temperature with MgO (100) tunnel barriers. *Nature Materials*, 3:862, 2004.

[20] T. Shiratori, E. Fujii, Y. Miyaoka, and Y. Hozumi. High-density magneto-optical recording with domain wall displacement detection. *Journal of the Magnetics Society of Japan*, 22(52):47, 1998.

[21] S. S. P. Parkin. Shiftable magnetic shift register and method of using the same. US Patent 6834005, 2004.

[22] D.A. Allwood, G. Xiong, M.D. Cooke, C.C. Faulkner, D. Atkinson, N. Vernier, and R.P. Cowburn. Submicrometer ferromagnetic NOT gate and shift register. *Science*, 296:2003, 2002.

[23] D.A. Allwood, G. Xiong, and R.P. Cowburn. Domain wall diodes in ferromagnetic planar nanowires. *Applied Physics Letters*, 85(14):2848, 2004.

[24] D.A. Allwood, G. Xiong, C.C. Faulkner, D. Atkinson, D. Petit, and R.P. Cowburn. Magnetic domain-wall logic. *Science*, 309:1688, 2005.

[25] M. Tsoi, R. E. Fontana, and S. S. P. Parkin. Magnetic domain wall motion triggered by an electric current. *Applied Physics Letters*, 83(13):2617–2619, 2003.

[26] G. S. D. Beach, C. Nistor, C. Knutson, M. Tsoi, and J. L. Erskine. Dynamics of field-driven domain-wall propagation in ferromagnetic nanowires. *Nature Materials*, 4:741–744, 2005.

[27] M. Redjdal, J. Giusti, M.F. Ruane, and F.B. Humphrey. Thickness dependent wall mobility in thin permalloy films. *Journal of Applied Physics*, 91:7547, 2002.

[28] T. Trunk, M. Redjdal, A. Kakay, M.F. Ruane, and F.B. Humphrey. Domain wall structure in Permalloy films with decreasing thickness at the Block to Néel transition. *Journal of Applied Physics*, 81:7606, 2001.

[29] A. Aharoni. Demagnetizing factors for rectangular ferromagnetic prisms. *Journal of Applied Physics*, 83(6):3432–3434, 1998.

[30] A. Thiaville, J. M. Garcia, and J. Miltat. Domain wall dynamics in nanowires. *Journal of Magnetism and Magnetic Materials*, 242:1061–1063, 2002.

[31] N. L. Schryer and L. R. Walker. The motion of 180 degree domain walls in uniform DC magnetic fields. *Journal of Applied Physics*, 45(12):5406, 1974.

[32] R. D. McMichael and M. J. Donahue. Head to head domain wall structures in thin magnetic strips. *IEEE Transactions on Magnetics*, 33(5):4167, 1997.

[33] Y. Nakatani, A. Thiaville, and J. Miltat. Head-to-head domain walls in soft nano-strips: A refined phase diagram. *Journal of Magnetism and Magnetic Materials*, 290-291:750, 2005.

[34] Y. Nakatani, A. Thiaville, and J. Miltat. Faster magnetic walls in rough wires. *Nature Materials*, 2:521, 2003.

[35] J.A. Katine, M.K. Ho, Y.S. Ju, and C.T. Rettner. Patterning damage in narrow trackwidth spin-valve sensors. *Applied Physics Letters*, 83(2):401, 2003.

[36] D. McGrouther and J.N. Chapman. Nanopatterning of a thin ferromagnetic CoFe film by focused-ion-beam irradiation. *Applied Physics Letters*, 87:022507, 2005.

[37] J. Fassbender and J. McCord. Control of saturation magnetization, anisotropy, and damping due to Ni implantation in thin $Ni_{81}Fe_{19}$ layers. *Applied Physics Letters*, 88:252501, 2006.

[38] G.T. Rado and A.R. Kaufmann. Absolute saturation magnetization of nickel-antimony and nickel-tantalum alloys. *Physical Review*, 60:336, 1941.

[39] B.X. Liu, W.S. Lai, and Q. Zhang. Irradiation induced amorphization in metallic multilayers and calculation of glass-forming ability from atomistic potential in the binary metal systems. *Material Science and Engineering R*, 29:1, 2000.

[40] L. Berger. Low-field magnetoresistance and domain drag in ferromagnets. *Journal of Applied Physics*, 49(3):2156, 1978.

[41] L. Berger. Exchange interaction between ferromagnetic domain-wall and electric-current in a very thin metallic-films. *Journal of Applied Physics*, 55(6):1954, 1984.

[42] G. Tatara and H. Kohno. Theory of current-driven domain wall motion: Spin transfer versus momentum transfer. *Physical Review Letters*, 92(8):086601, 2004.

[43] Z. Li and S. Zhang. Domain-wall dynamics and spin-wave excitations with spin-transfer torques. *Physical Review Letters*, 92(20):207203, 2004.

[44] S. Zhang and Z. Li. Roles of nonequallibrium conduction electrons on the magnetization dynamics of ferromagnets. *Physical Review Letters*, 93(12):127204, 2004.

[45] A. Thiaville, Y. Nakatani, J. Miltat, and Y. Suzuki. Micromagnetic understanding of current-driven domain wall motion in patterned nanowires. *Europhysics Letters*, 69(6):990, 2005.

[46] S.E. Barnes and S. Maekawa. Current-spin coupling for ferromagnetic domain walls in fine wires. *Physical Review Letters*, 95(10):107204, 2005.

[47] P.P. Freitas and L. Berger. Observation of s-d exchange force between domain walls and electric current in very thin Permalloy films. *Journal of Applied Physics*, 57(4):1266, 1985.

[48] L. Berger. Motion of a magnetic domain wall traversed by fast-rising current pulses. *Journal of Applied Physics*, 71(6):2721, 1992.

[49] N. Vernier, D.A. Allwood, D. Atkinson, M.D. Cooke, and R.P. Cowburn. Domain wall propagation in magnetic nanowires by spin-polarized current injection. *Europhysics Letters*, 65(4):526, 2004.

[50] M. Kläui, P.-O. Jubert, R. Allenspach, A. Bischof, J.A.C. Bland, G. Faini, U. Rüdiger, C.A.F. Vaz, L. Vila, and C. Vouille. Direct observation

of domain-wall configurations transformed by spin currents. *Physical Review Letters*, 95(2):026601, 2005.

[51] G. S. D. Beach, C. Knutson, C. Nistor, M. Tsoi, and J. L. Erskine. Nonlinear domain-wall velocity enhancement by spin-polarized electric current. *Physical Review Letters*, 97(5):057203, 2006.

[52] J. He, Z. Li, and S. Zhang. Current-driven vortex domain wall dynamics by micromagnetic simulation. *Physical Review B*, 73:184408, 2006.

[53] G. S. D. Beach, C. Knutson, M. Tsoi, and J. L. Erskine. Field- and current-driven domain wall dynamics: An experimental picture. *Journal of Magnetism and Magnetic Materials*, 310:2038, 2007.

[54] S. Yang and J. L. Erskine. Domain wall dynamics and Barkhausen jumps in thin-film permalloy microstructures. *Physical Review B*, 72:064433, 2005.

[55] D. Ravelosona, F. Cayssol, J. Wunderlich, H.W. Schumacher, C. Chappert, V. Mathet, J. Ferré, and J.-P. Jamet. Dynamics of magnetization reversal in a mesoscopic wire. *Journal of Magnetism and Magnetic Materials*, 249:170, 2002.

[56] L. Berger. Possible existence of a Josephson effect in ferromagnets. *Physical Review B*, 33(3):1572, 1986.

Vita

Carl Oliver Knutson was born in Minneapolis, Minnesota on 27 February 1980, the son of L. Timothy Knutson and Jeanette L. Knutson. After completing his work at the High School for Science and Engineering Professions at Dunbar High School, Fort Worth, TX, in 1998, he entered Haverford College in Haverford, PA. He received the degree of Bachelor of Science in Physics from Haverford College in May 2002. In August 2002 he entered the Graduate School at the University of Texas at Austin.

Permanent address: 11905 Snow Goose Road
Austin, Texas 78758

This dissertation was typeset with LaTeX[†] by the author.

[†]LaTeX is a document preparation system developed by Leslie Lamport as a special version of Donald Knuth's TeX Program.